

Hybrid quantum systems with trapped charged particles

Shlomi Kotler,^{*} Raymond W. Simmonds, Dietrich Leibfried, and David J. Wineland
National Institute of Standards of Technology, 325 Broadway St., Boulder, Colorado 80305, USA
 (Received 9 August 2016; published 21 February 2017)

Trapped charged particles have been at the forefront of quantum information processing (QIP) for a few decades now, with deterministic two-qubit logic gates reaching record fidelities of 99.9% and single-qubit operations of much higher fidelity. In a hybrid system involving trapped charges, quantum degrees of freedom of macroscopic objects such as bulk acoustic resonators, superconducting circuits, or nanomechanical membranes, couple to the trapped charges and ideally inherit the coherent properties of the charges. The hybrid system therefore implements a “quantum transducer,” where the quantum reality (i.e., superpositions and entanglement) of small objects is extended to include the larger object. Although a hybrid quantum system with trapped charges could be valuable both for fundamental research and for QIP applications, no such system exists today. Here we study theoretically the possibilities of coupling the quantum-mechanical motion of a trapped charged particle (e.g., an ion or electron) to the quantum degrees of freedom of superconducting devices, nanomechanical resonators, and quartz bulk acoustic wave resonators. For each case, we estimate the coupling rate between the charged particle and its macroscopic counterpart and compare it to the decoherence rate, i.e., the rate at which quantum superposition decays. A hybrid system can only be considered quantum if the coupling rate significantly exceeds all decoherence rates. Our approach is to examine specific examples by using parameters that are experimentally attainable in the foreseeable future. We conclude that hybrid quantum systems involving a single atomic ion are unfavorable compared with the use of a single electron because the coupling rates between the ion and its counterpart are slower than the expected decoherence rates. A system based on trapped electrons, on the other hand, might have coupling rates that significantly exceed decoherence rates. Moreover, it might have appealing properties such as fast entangling gates, long coherence, and flexible topology that is fully electronic in nature. Realizing such a system, however, is technologically challenging because it requires accommodating both a trapping technology and superconducting circuitry in a compatible manner. We review some of the challenges involved, such as the required trap parameters, electron sources, electrical circuitry, and cooling schemes in order to promote further investigations towards the realization of such a hybrid system.

DOI: [10.1103/PhysRevA.95.022327](https://doi.org/10.1103/PhysRevA.95.022327)

I. INTRODUCTION

Trapping of charged particles [1,2] has enabled long interrogation times of their external and internal states, enabling precision metrology, such as atomic clocks. Applying these tools to atomic ions, paired with laser-enabled state manipulation, can also turn ions into a quantum information processing (QIP) platform [3–7]. Ions have demonstrated record fidelities for initialization, readout, individual spin manipulation [8], and entanglement [9,10].

Other quantum-coherent systems might therefore benefit, by coupling to trapped ions, potentially inheriting aspects of their high controllability and coherence. For example, as described below, we might be able to use a single ${}^9\text{Be}^+$ ion coupled to a ~ 10 mg quartz resonator to cool the latter close to its ground state. By placing the ion in a superposition state of motion and transferring it to a macroscopic resonator, we could explore bounds on quantum mechanics for massive objects. The ion therefore could provide a “quantum transducer” that enables the manipulation of a much larger object in a coherent way at the single-phonon level. For the purpose of QIP, ions might be used as excellent memory units, e.g., for superconducting devices, as long as quantum information can be exchanged between the two systems on timescales that are sufficiently short compared

with the decoherence time of the superconducting circuit. The internal degrees of freedom of an ion can remain coherent for tens to hundreds of seconds [8,11–13], significantly exceeding the lifetime of coherent excitation in current superconducting devices, typically limited to less than $100 \mu\text{s}$ (see, e.g., Ref. [14]), setting the timescale for useful quantum exchange.

The resonant interaction of ions with radio frequency electrical resonators was studied in Ref. [15]. Complementary parametric interaction schemes for the nonresonant case were studied in Refs. [16–20]. Other suggestions include interfacing nanomechanical resonators [21–25], electrical wires [26], and superconducting qubits [25]. These reports analyzed the basic physics involved in each of the different coupling mechanisms as well as the prospects of using such hybrid systems.

Here, we focus on a few specific examples of hybrid systems rather than presenting a general treatment. For these examples we take into account available materials, achievable quality factors, and practical limitations. Nevertheless, our analysis is based on a unified framework (Sec. II) that allows for direct comparison of relevant figures of merit associated with the different systems. We hope these examples are representative of the different opportunities available and can illuminate some of the issues of hybrid QIP with charged particles.

A charged particle moving in a harmonic trap gives rise to an oscillating electric dipole. This dipole in turn can couple

^{*}shlomi.kotler@nist.gov

to nearby charged objects [21,27,28], generate image currents in a nearby conductor [15], polarize a dielectric material, or induce motion in a piezoelectric crystal. If the coupled system also has a harmonic mode resonant with the ion motion, energy exchange will occur between the ion harmonic motion and the coupled system.

The analysis that follows below is guided by the realization that coupling two quantum systems is a double-edged sword. Ideally, we would like to benefit from the useful properties of both systems. In reality, the hybrid system often inherits the disadvantages of both constituents. Therefore, to retain any useful quantum characteristics, we require that the coupling rate between the two systems exceeds the fastest relevant decoherence rate in both systems. Additionally, we focus on specific architectures where the two technologies involved could be compatible and not preclude either of the coupled systems from being close to a pure quantum state.

Although we cannot completely rule out all mechanisms considered here that involve an atomic ion, the analysis emphasizes how challenging it would be to incorporate ions into a hybrid system at the quantum level. The coupling rates we calculate, based on experimentally attainable parameters, are either well below the decoherence rates or marginally close to them. This conclusion changes when considering coupling a charged particle to a superconducting resonator, assuming an electron rather than an ion (e.g., see Refs. [15,18,29,30] as well as Sec. VI for a more extensive reference list). This follows from the fact that for a particle of mass m the coupling rate is proportional to $m^{-1/2}$ (see Sec. IV), rendering coupling rates for an electron on the order of ~ 0.1 to 1 MHz, where we expect to exceed decoherence rates.

The shift from using an atomic ion to using an electron has significant practical implications, as detailed in Sec. VI. Laser-enabled state manipulation, specifically laser cooling, plays an important role in trapped atomic ion QIP experiments. Without these tools, electrical-circuit-based alternatives need to be considered along with their implications on the system as a whole. We therefore embark on a feasibility study that takes these implications into account, considering among other factors trap stability, trap depth, maintaining superconductivity, the requirements from a low-energy electron source, electrical wiring, and the superconducting resonator involved. A previous report [18] has already suggested a specific electron trap that would support a parametric coupling scheme. The different aspects considered in the feasibility study bear significance on the trap design, suggesting that a larger trap be used for an electron-based hybrid system.

Although technically challenging, these issues do not seem to preclude a hybrid system based on a trapped electron. As detailed in Sec. VI, such a platform might offer appealing qualities such as fast entangling gates (~ 10 ns) and long coherence times (seconds), rendering a coherence time to gate time ratio of $\geq 10^8$, far exceeding any current QIP system. Moreover, the platform could offer a flexible coupling topology enabled by interfacing engineered electrical circuits, potentially enabling high-fidelity electron spin readout. This, in turn, could open new avenues of basic research, interesting in their own right.

II. ELECTRICAL EQUIVALENT OF MECHANICAL MOTION

There are various systems that could, in principle, couple to a trapped charged particle. Those systems differ from the charged particle and from one another in frequency, mass, length scale, and coupling mechanism, as highlighted in Fig. 1. With the exception of the electrical LC resonator, all other systems considered here are mechanical resonators actuated by an electromagnetic field. To place all of them on an equal footing we associate an electrical equivalent for each of these mechanical systems. This reduces the analysis of any of the hybrid systems into an all-electrical circuit problem. Our discussion extends the treatment in Ref. [31] where the electrical equivalent circuit of a trapped ion was derived. This could also be derived by using the general framework developed by Butterworth and Van Dyke [32–34] that associates a circuit equivalent for electrically actuated mechanical systems. We refer to the resulting electrical network as the BVD equivalent circuit.

Suppose a mechanical system of mass m is placed near an electrode that is biased with voltage V , resulting in a force $F = \beta V$ acting on it. For simplicity, we assume the geometry in Fig. 2(a), where two electrodes form the two plates of a parallel plate capacitor, separated by a distance d . An important example (analyzed in Refs. [31,35]) is that of a single charged particle with charge q resulting in $F = qV/d$, i.e., $\beta = q/d$. In general, electrical actuation could also result from dipolar interaction, electrostriction, piezoelectricity, etc. Since microscopically these mechanisms originate from having nonzero local charge densities within the mechanical system, we lump the overall effect of the voltage with a single effective parameter β .

When the mass m moves at velocity v [see Fig. 2(b)], it will induce a current $I = \beta v$ at the electrode. This is an immediate generalization of the single-charged-particle case: if it is at a distance x from an electrode it induces an image charge of $q_{\text{image}} = qx/d$. Therefore, within the electrostatic approximation, a velocity $v = \dot{x}$ would translate into a current $I = qv/d$. The induced charges will back-act on the mass m with an additional force ΔF . This force, however, will be independent of V and will not contribute to the induced current I . The effect of ΔF can therefore be lumped into a (usually but not necessarily) small change of the system's mechanical properties, e.g., its spring constant in the case of a harmonic oscillator (for a rigorous derivation see Refs. [31,35]).

Now assume that the mechanical system is harmonic, i.e., that it has a resonant frequency ω_0 and a friction coefficient γ . If the voltage is time varying, $V(t)$, the equation of motion for the harmonic-oscillator position x is

$$m\ddot{x} + \gamma\dot{x} + m\omega_0^2x = \beta V(t). \quad (1)$$

By using the relation $I(t) = \beta\dot{x}$ this can be rewritten as

$$\frac{m}{\beta^2} \frac{dI}{dt} + \frac{\gamma}{\beta^2} I + \frac{m\omega_0^2}{\beta^2} \int^t dt' I(t') = V(t). \quad (2)$$

Therefore, from the perspective of the electrical circuit, the mechanical system is equivalent to a series combination of

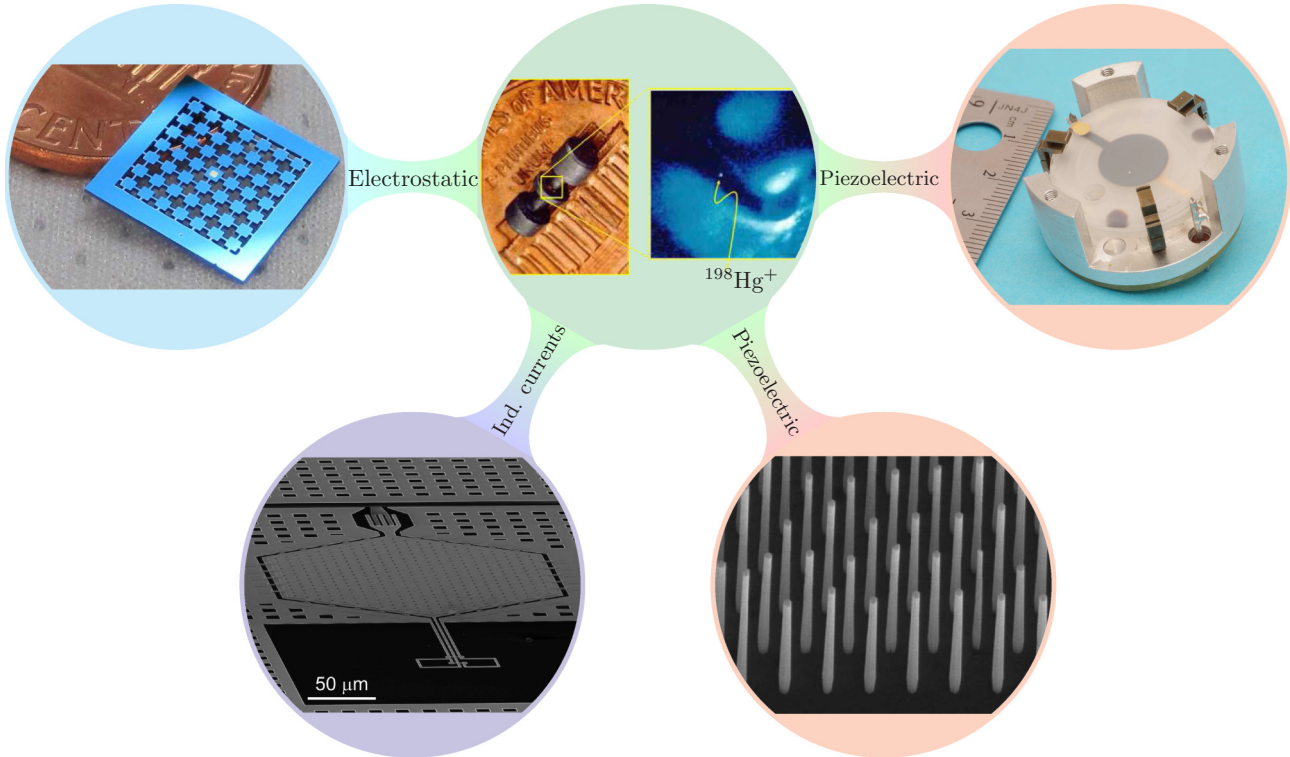


FIG. 1. Examples of different platform candidates for a hybrid architecture considered in this paper. Clockwise from the top-middle: $^{198}\text{Hg}^+$ ion trap, quartz bulk acoustic wave resonator, gallium nitride nanobeams, superconducting LC circuit, and nanomechanical silicon nitride (SiN) membrane. The ion (green shading) is coupled via piezoelectricity (red shading), induced image currents (purple shading) or electrostatics (blue shading). Ion trap photograph courtesy of J. Bergquist, NIST, Boulder, Colorado 80305, USA. Gallium nitride nanobeams photographs courtesy of K. Bertness, NIST, Boulder, Colorado 80305, USA. Quartz resonator device courtesy of S. Galliou, FEMTO-ST institute, 25000 Besançon, France. SiN membrane photograph courtesy of K. Cicak, NIST, Boulder, Colorado 80305, USA.

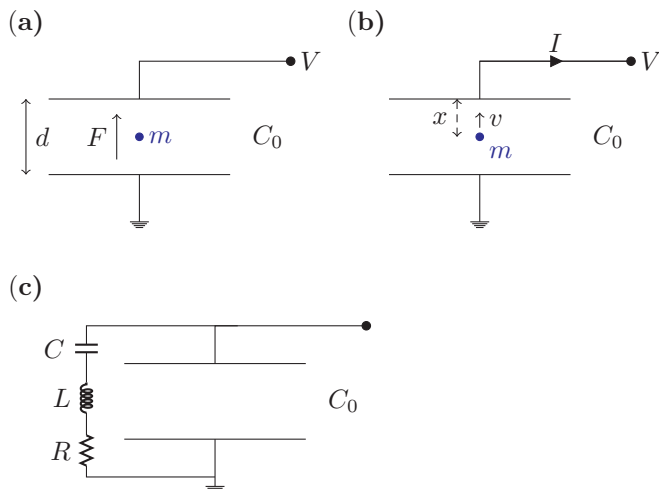


FIG. 2. Simplified geometry for an electrically actuated mechanical system. (a) A mechanical system of mass m is placed inside a capacitor C_0 that is biased at a voltage V . The force acting on m is assumed to be proportional to the capacitor bias voltage $F = \beta V$. (b) If the mechanical system velocity is $v \neq 0$ an image current $I = \beta v$ is induced. (c) BVD equivalent circuit. The mechanical system electrical response is identical to that of a series RLC circuit connected in parallel with the capacitor C_0 .

resistance, inductance, and capacitance; namely,

$$L \frac{dI}{dt} + RI + \frac{1}{C} \int^t dt' I(t') = V(t), \quad (3)$$

where

$$L \leftrightarrow \frac{m}{\beta^2}, \quad R \leftrightarrow \frac{\gamma}{\beta^2}, \quad C \leftrightarrow \frac{\beta^2}{m\omega_0^2}, \quad (4)$$

and their series combination is added in parallel to the capacitance of the drive electrode C_0 [see Fig. 2(c)].

Throughout this paper, we refer to the mechanical system and its electrical equivalent interchangeably, in order to simplify the coupling analysis.

III. COUPLING IN STRONG QUANTUM REGIME

Our general problem is concerned with two resonantly coupled harmonic oscillators (mechanical or electrical). We assume that the coupling rate g is much smaller than the frequencies of the harmonic oscillators so that the coupling Hamiltonian can be treated perturbatively. The Hamiltonian coupling term for two mechanical harmonic oscillators of masses m_1 , m_2 and bare frequencies ω'_1 , ω'_2 by a spring of constant k [Fig. 3(a)] is

$$H_c = kx_1x_2, \quad (5)$$

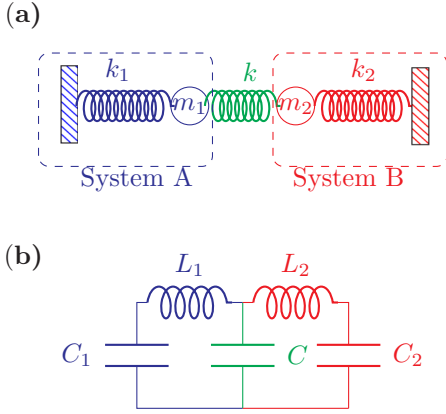


FIG. 3. (a) Coupled mechanical harmonic oscillators. (b) Coupled electrical harmonic oscillators.

where x_1 and x_2 are the displacements of the oscillators from equilibrium. The resonant frequency for each of the harmonic oscillators in the presence of the coupling spring is $\omega_i = (\omega_i^2 + k/m_i)^{1/2}$. If $\omega_1 = \omega_2 = \omega_0$ the coupling Hamiltonian can be rewritten in terms of a coupling rate g by expressing x_i in terms of their respective harmonic-oscillator ladder operators $x_i = \sqrt{\hbar/(2m_i\omega_i)}(\hat{a}_i + \hat{a}_i^\dagger)$ so that

$$H_c = \hbar g (\hat{a}_1 + \hat{a}_1^\dagger)(\hat{a}_2 + \hat{a}_2^\dagger), \quad (6)$$

where

$$g = \frac{k}{2\omega_0\sqrt{m_1m_2}}, \quad (7)$$

and \hbar is the Planck constant divided by 2π .

It will be useful later to express g in terms of an analog electrical system [Fig. 3(b)] of two LC resonators coupled by a shunt capacitor C . In this case, the coupling Hamiltonian is

$$H_c = \frac{1}{C} q_1 q_2, \quad (8)$$

where q_1 and q_2 are the charges on the capacitors C_1 and C_2 , respectively. The resonant frequency for each of the LC resonators is $\omega_i = 1/\sqrt{L_i C_i'}$ where $C_i' = C_i C / (C_i + C)$ is the series capacitance of C_i and C . Assuming $\omega_1 = \omega_2 = \omega_0$, we can rewrite Eq. (8) in terms of the ladder operators, $q_i = \sqrt{\hbar\omega_0 C_i' / 2} (a_i + a_i^\dagger)$, so that H_c takes the form of Eq. (6) with

$$g = \frac{\omega_0}{2} \sqrt{\frac{C_1 C_2}{(C_1 + C)(C_2 + C)}}. \quad (9)$$

We stress that both Eqs. (7) and (9) are valid only if the coupling rate g is smaller than the harmonic oscillator's frequency, i.e., $g \ll \omega_0$.

We will be particularly interested in the *strong-coupling quantum regime*, i.e., when a large number of complete energy oscillations occur between the two oscillators before they significantly lose coherence: $N_{\text{osc}} \approx \tau_{\text{coh}}/\tau_{\text{osc}} \gg 1$. Here $\tau_{\text{osc}} = \pi/g$ is the time required for a complete energy oscillation (back and forth) between the two oscillators. For a system of two harmonic oscillators, τ_{coh} is the average exchange period of a single energy quantum with any of the thermal baths of the oscillators. We assume that coherence is

limited by energy relaxation. In reality, there are additional decoherence mechanisms that could decrease N_{osc} further and the values calculated here should be considered as an upper bound. An important case is motional dephasing of a trapped charged particle [21,36]. Although the motional heating rate for trapped ions could be as low as a few quanta per second (see Appendix B), trap-frequency drifts, for example, could cause motional dephasing at a higher rate. Another well-known source of motional decoherence is the nonlinear coupling between trap axes due to trap imperfections [21]. Although these mechanisms could be reduced by technical means, it would be highly favorable from a practical standpoint that the coupling strength $g \geq 2\pi \times 1$ kHz, posing an additional constraint in what follows.

When expressing the above condition in terms of the *lower* of the two quality factors Q associated with the two oscillators and the temperature T of their environment, we observe two regimes. At “high” temperatures ($k_B T \geq \hbar\omega_0$), the thermal equilibration time constant $\tau_{\text{thermal}} = Q/\omega_0$ of the oscillators can be thought of as the $1/e$ time required to heat the mechanical oscillator from 0 K to the surrounding temperature T , i.e., the time it takes to acquire an average of $(1 - 1/e)n_{\text{thermal}}$ phonons where $n_{\text{thermal}} = [\exp(\frac{\hbar\omega_0}{k_B T}) - 1]^{-1} \approx \frac{k_B T}{\hbar\omega_0}$ energy quanta and k_B is the Boltzmann constant. Any quantum coherent phenomena will therefore be restricted to times shorter than $\tau_{\text{coh}} = \tau_{\text{thermal}}/n_{\text{thermal}} \approx \hbar Q/k_B T$, roughly the time required to absorb one phonon at the rate of thermal equilibration. At “low” temperatures ($k_B T \leq \hbar\omega_0$) the equilibrated oscillator contains one phonon or less on average and therefore $\tau_{\text{coh}} = Q/\omega_0$. The strong quantum regime condition therefore translates to

$$N_{\text{osc}} \approx \frac{gQ}{\pi(n_{\text{thermal}} + 1)\omega_0} \gg 1. \quad (10)$$

At typical liquid-helium temperatures of ~ 4 K, $k_B T/\hbar = 2\pi \times 83$ GHz, so for frequencies below 83 GHz we require

$$N_{\text{osc}} \approx \frac{gQ}{2\pi \times 262 \text{ GHz}} \gg 1. \quad (11)$$

For dilution-refrigerator temperatures of ≤ 50 mK for example, $k_B T/\hbar = 2\pi \times 1$ GHz, so for frequencies below 1 GHz we require

$$N_{\text{osc}} \approx \frac{gQ}{2\pi \times 3.3 \text{ GHz}} \gg 1. \quad (12)$$

The inequalities in Eqs. (10)–(12) introduce stringent constraints both on the coupling strength g and the Q factors involved. The need for high Q factors accounts for why superconducting circuits, which often have high Q factors, naturally arise in the context of hybrid systems, as will be seen in the next section.

If the two oscillators have different eigenfrequencies ($\omega_1 \neq \omega_2$) their weak off-resonant coupling could be brought into a strong effective resonant coupling by modulating one or more of the system parameters by a fraction $0 < \eta < 1$, at the difference frequency, $\omega_1 - \omega_2$, usually at the expense of a lower coupling rate. For example, if the two mechanical oscillators in Fig. 3(a) have different resonant frequencies,

they can still be coupled by modulating the spring constant k at the difference frequency. The expression for the coupling rate in Eq. (6) generalizes to $g = \eta k / (4\sqrt{\omega_1 \omega_2 m_1 m_2})$. Therefore, the coupling strength is reduced by $\eta/2$, where η is typically at the 0.05 to 0.2 range to avoid nonlinear behavior of the coupling spring. We note that parametric schemes can have certain advantages. For example, by coupling a low-frequency resonator to a high-frequency resonator, a low number of phonon or photon occupancy for the low-frequency resonator can be achieved which could be useful for experiment initialization, for example. This, however, does not improve the coherence time of either system unless they are coupled to different thermal baths with different temperatures (e.g., see Ref. [37]). Since large coupling rates compared with decoherence rates are critical, we concentrated on resonant oscillators in the above discussion and in what follows. For details of parametric coupling schemes in the context of hybrid systems involving ions, see Refs. [17–20].

IV. TRAPPED CHARGED PARTICLE COUPLED TO AN ELECTRICAL RESONATOR

The first hybrid system we consider is that of a trapped charged particle coupled to an electrical resonator, following Ref. [15] (see also Ref. [25]). Schematically, a point particle of mass m and charge q is elastically bound by a trap, here modeled by a spring (see Fig. 4), with a resonant radial frequency ω_0 . If the particle is placed between the two plates of a capacitor, any voltage difference V between the plates would result in a force $F = \alpha q V / d$ acting on it, where d is the distance between the plates and α is a unitless geometric factor ($\alpha = 1$ for a parallel plate capacitor with infinite plate areas). The equivalent electrical circuit [Eq. (4)] is composed of an effective inductance L_p and capacitance C_p , where

$$L_p = \frac{m d^2}{\alpha^2 q^2}, \quad C_p = \frac{1}{L_p \omega_0^2}. \quad (13)$$

Therefore, the hybrid system composed of a harmonically confined charged particle and resonator is equivalent to a lumped element LC circuit (L_p, C_p) shunted by the trap capacitance C_{trap} and coupled to the electrical resonator, as shown in Fig. 4(b). From Eq. (9) and assuming $C \gg C_{\text{trap}}$ for

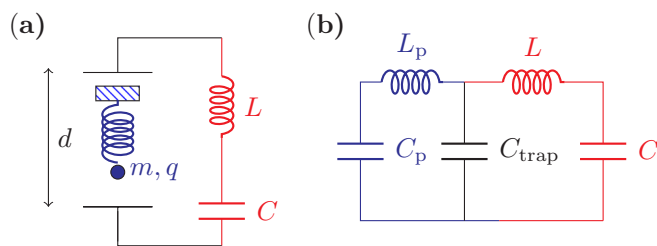


FIG. 4. (a) A simplified picture of a trapped particle coupled to an LC resonator. (b) The corresponding electrical BVD equivalent circuit. The trap capacitance C_{trap} in panel (b) is formed by the two equivalent parallel plates, which are a distance d from one another in panel (a).

maximal coupling, we get

$$g = \frac{\omega_0}{2} \sqrt{\frac{C_p}{C_{\text{trap}}}} = \frac{\alpha q}{2d} \frac{1}{\sqrt{m C_{\text{trap}}}}. \quad (14)$$

Notice that this is an upper bound on the coupling rate g . In any realistic implementation, the two trap electrodes need to be dc biased independently and therefore a finite value of C should be taken into account.

This coupling can be increased by trapping more than one charged particle. If N_p particles are trapped and form a Wigner crystal, their common mode motion can be treated as that of a single particle with a charge of $N_p q$ and a mass of $N_p m$. From Eq. (14) it follows that $g \propto \sqrt{N_p}$. For very small traps however, N_p will be limited by the Coulomb repulsion between the charges.

Based on Eq. (10), Table I summarizes the constraints on the Q factor of the electrical resonator required to be in the strong-coupling quantum regime for various charged particles. These should be compared with experimentally attainable values for lumped-element superconducting resonators that are typically in the range of $Q \sim 10^4$ – 10^5 and in some cases up to 10^6 , mostly limited by dielectric losses [14,38]. Since the required Q is greater than these values, achieving strong coupling of an ion to a superconducting resonator at 4 K does not seem feasible. In fact, the only two candidates from Table I that stand out in terms of reasonable Q factors are ${}^9\text{Be}^+$ ($Q \gg 7 \times 10^5$ at 50 mK) and electrons ($Q \gg 4 \times 10^5$ at 4 K and $Q \gg 7 \times 10^3$ at 50 mK). For ${}^9\text{Be}^+$ it would require incorporating atomic ion trapping technology into a dilution refrigerator, the discussion of which is beyond the scope of this paper and can be found elsewhere [20]. We discuss the prospects of electron coupling in the last part of the paper. Our estimates are compatible with previous results [18,26].

In the above discussion we considered only lumped-element electrical resonators. A different approach would be to use low frequency transmission line resonators. Those can be simpler to fabricate and could potentially have higher quality factors. As an example, Fig. 5(a) shows a simple geometry where an ion is trapped close to the voltage antinode of a quarter-wave resonator. Near resonance, the transmission line resonator is equivalent to a parallel LC circuit [see Fig. 5(b)] with effective capacitance $C = \pi / (4\omega_0 Z_0)$ and inductance $L = 1 / (\omega_0^2 C)$ where ω_0 is the resonance frequency and Z_0 is the characteristic impedance of the transmission line [39]. The coupling strength is calculated, as before, by using the electrical equivalent circuit

$$g = \frac{\omega_0}{2} \sqrt{\frac{C_p}{C + C_{\text{trap}}}}. \quad (15)$$

The main concern is that the effective capacitance C of these resonator modes is very large. For a typical $Z_0 = 50$ ohm transmission line and $\omega_0 = 2\pi \times 10$ MHz, $C \sim 250$ pF. The coupling strength g will therefore degrade by a factor of ~ 70 as compared with the numbers in Table I, requiring, for example, a quality factor satisfying $Q \gg 4 \times 10^9$ for ${}^9\text{Be}^+$ at 4 K. This number exceeds the best quality factors for such resonators, having $Q \sim 10^7$ at 10 MHz [40]. Moreover, our estimate for g is an upper bound since, in a real geometry, the field lines at

TABLE I. Coupling strengths of different trapped charged particles coupled to an electrical resonator. The mass of the proton and the electron are m_p and m_e , respectively. We assume the geometry in Fig. 4, with $d = 50 \mu\text{m}$, $C_{\text{trap}} = 50 \text{ fF}$, and $\alpha = 1$, and use Eq. (14) to calculate g . The table states a lower bound for the required Q factors; namely, Q corresponding to $N_{\text{osc}} = 1$. Actual Q factors should be at least an order of a magnitude greater to comfortably satisfy inequality (10). These estimates are consistent with Ref. [26], where 600 Hz coupling strength was estimated for $^{40}\text{Ca}^+$ in a 1 MHz trap with 2.5 pF trap capacitance, $d = 50 \mu\text{m}$, and $\alpha = 1$. Our trap-capacitance estimate of $C_{\text{trap}} = 50 \text{ fF}$ can only be achieved in small trap geometries through careful design (see, for example, Sec. VIA). Moreover, additional capacitors required for the trap circuit operation may add to the total capacitance resulting in a lower coupling strength (see Sec. VIE). The values for g here, therefore, should be considered as an upper bound estimate.

Particle	Mass, m	Trap frequency, ω_0	Coupling strength, g	Q_{min} (4 K)	Q_{min} (50 mK)
Electron	m_e	1.3 GHz	1.2 MHz	4×10^5	7×10^3
$^9\text{Be}^+$	$9m_p$	10 MHz	9 kHz	56×10^6	7×10^5
$^{24}\text{Mg}^+$	$24m_p$	6 MHz	6 kHz	92×10^6	1.1×10^6
$^{40}\text{Ca}^+$	$40m_p$	4.7 MHz	4 kHz	119×10^6	1.5×10^6
$^{88}\text{Sr}^+$	$88m_p$	3.2 MHz	3 kHz	176×10^6	2×10^6

the voltage antinode of the resonator will differ from those of an ideal parallel plate capacitor. For these reasons, our analysis has focused on coupling the charged particle to a lumped-element electrical oscillator, where the same resonant frequency can usually be achieved with significantly less overall capacitance.

V. COUPLING TO MACROSCOPIC MECHANICAL RESONATORS

To circumvent the limitations of attainable Q factors of superconducting devices, it has been suggested to try and couple an ion directly to a high- Q macroscopic mechanical object by using electrostatic coupling [15,21,23–25] or piezoelectricity [15,41].

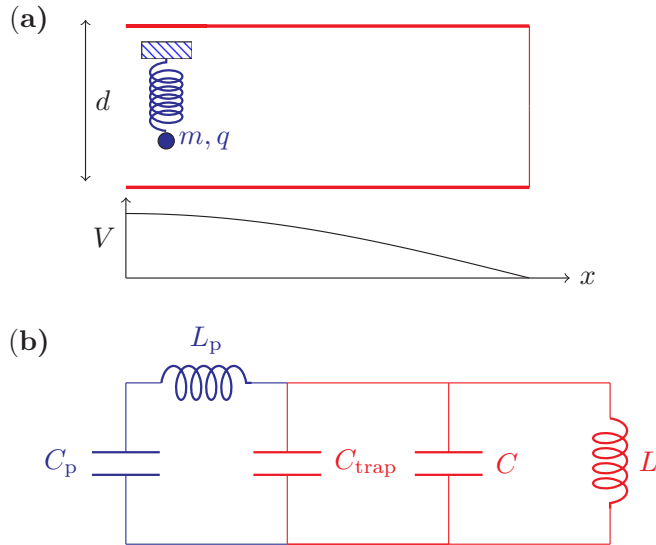


FIG. 5. (a) A simplified picture of a trapped ion coupled to a transmission line resonator. The ion is trapped close to the voltage antinode of a short-circuited quarter-wave resonator. (b) The corresponding electrical equivalent circuit. The ion is replaced with its equivalent series capacitance C_p and inductance L_p while the resonator is replaced with its equivalent lumped element representation formed by a parallel LC resonator. Additional capacitance due to trap electrodes is represented by C_{trap} .

A. Electrostatic coupling to a nanomechanical membrane

Commercial nanomechanical membrane resonators can have high quality factors, over 10^7 at 300 mK [42]. Recent advances in membrane fabrication [43–47] have resulted in quality factors as high as 10^8 , even at room temperature. If such a membrane is metalized on one side, and biased with a voltage U , it could electrostatically couple to an ion trapped near its surface. To estimate this coupling, we assume the simple geometries shown in Fig. 6. In both cases, the coupling Hamiltonian is

$$H = \alpha q U \frac{z_i z_m}{d_0^2}, \quad (16)$$

where z_i , z_m are the displacements of the ion z motion and the membrane, respectively, d_0 is the distance between the membrane and the bottom electrode of the ion trap, and α is a geometric factor as in Sec. IV. For the geometries considered here, $0.5 \leq \alpha \leq 1$ and we assume $\alpha = 1$ to get an upper bound for g . As in Eq. (6), we can derive the coupling strength

$$g = \frac{\alpha q U}{2d_0^2 \omega_0 \sqrt{m_{\text{ion}} M}}, \quad (17)$$

where M is the membrane mode mass and ω_0 its resonant frequency. These masses are significantly larger than the ion

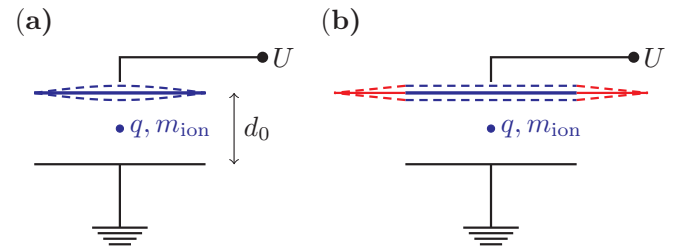


FIG. 6. Electrostatic coupling of a trapped ion (charge q and mass m_{ion}) to a nearby rectangular nanomechanical membrane biased by a voltage U . The ion is assumed to be trapped at a height $d_0/2$ above a surface trap, which is dc grounded with respect to the membrane, suspended above the ion (for simplicity the trap rf electrodes are omitted). (a) A membrane (blue) is clamped at its rim, allowing for a sinusoidal fundamental mode as in Ref. [43]. (b) A membrane (blue) is attached by thin wires (red), allowing for a center-of-mass fundamental mode as in Refs. [45,46].

mass, thereby lowering the coupling strength, with a mass ratio on the order of $M/m_{\text{ion}} \sim 10^{14}$ for ${}^9\text{Be}^+$. We assume that $d_0 = 100 \mu\text{m}$ and the ion is trapped midway between the membrane and the trap. For a SiN membrane [43] with dimensions $500 \mu\text{m} \times 500 \mu\text{m}$, coupled to a ${}^9\text{Be}^+$ ion, we get a mode mass of $M \sim 2 \times 10^{-11} \text{kg}$, a resonant frequency $\omega \sim 2\pi \times 1 \text{MHz}$, and a coupling strength of $g/2\pi \sim 0.24 \text{Hz}$ at $U = 1 \text{V}$ bias. Combined with an assumed quality factor of 2×10^8 , such a device does not satisfy the strong quantum criteria at $T = 50 \text{mK}$ since $gQ/2\pi \sim 0.048 \text{GHz}$ [see Eq. (12)]. For a suspended trampoline membrane [45,46] with dimensions $100 \mu\text{m} \times 100 \mu\text{m}$, coupled to a ${}^9\text{Be}^+$ ion, we get a mode mass of $M \sim 10^{-12} \text{kg}$, a resonant frequency of $\omega \sim 2\pi \times 140 \text{kHz}$, and a coupling strength of $g/2\pi \sim 12 \text{Hz}$ at $U = 1 \text{V}$, leading to $gQ/2\pi \sim 1.2 \text{GHz}$. The latter nearly enters the strong quantum regime for $T = 50 \text{mK}$. However, taking into account ion heating rates still makes this scheme unfavorable, because ion motional heating rate and motional dephasing would typically exceed g .

The coupling can be made stronger by increasing the bias voltage U at the expense of changing the trapping potential, the ion position, and possibly the trapping stability. Even with the $U = 1 \text{V}$ assumed above, the equilibrium position of, say a ${}^9\text{Be}^+$ ion in a 10MHz harmonic trap, would move by $\sim 7 \mu\text{m}$. This might be mitigated by adding additional electrodes that compensate for the static voltage bias effect of the membrane (e.g., see Ref. [25]). Those electrodes, however, might shield some of the trapping field and need to be taken into account when estimating the ion-trapping potential. In addition, a more careful estimation of g would take the membrane mode shape and finite size into account. Finally, adding an electrode to a membrane might decrease its Q factor. Previous experiments [48] with lower quality factors ($Q \sim 10^6$) showed that metallization of the membrane was not the limiting factor. Whether this is also true for the case of $Q \sim 10^8$ would need to be tested experimentally.

B. Piezoelectric coupling to acoustic resonator

A piezoelectric resonator is an acoustic resonator made from piezoelectric materials and can therefore be excited by using external electric fields [49]. Quartz resonators have been optimized for stable frequency operation and are therefore natural candidates for ion coupling, despite being relatively massive. A different plausible candidate is GaN-nanobeams that have low masses.

To estimate the coupling strength, we start by considering the geometry shown in Fig. 7. An ion is trapped at a distance h above a GaN nanobeam. Such an arrangement can be achieved, for example, by bringing a surface ion trap [50,51] or a stylus ion trap [52,53] close to the beam. The main challenge would seem to be to compensate for electric fields from stray charges on the dielectric beam due to its close proximity. We assume throughout that those are compensated for. When such a beam undergoes small oscillations, the position of each point in the beam can be written as $\vec{r} + \vec{u}(\vec{r}, t)$ where $\vec{r} = (r_1, r_2, r_3)$ is the equilibrium position and $\vec{u} = (u_1, u_2, u_3)$ is the time-dependent displacement from equilibrium. In a flexure acoustic mode, \vec{u} is along the \hat{r}_3 direction and its spatial dependence is restricted to the first component of \vec{r}

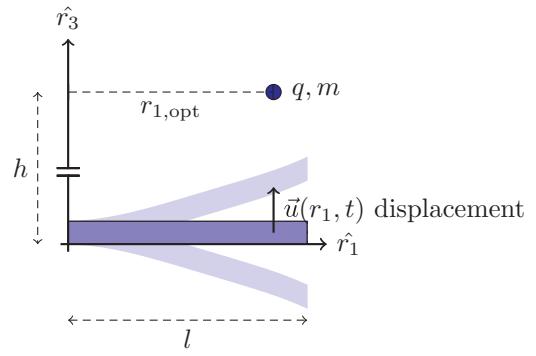


FIG. 7. Piezo coupling between an ion of mass m and charge q to a nanobeam. The ion is held at a height h above a beam of length l by a Paul trap (not shown). The geometry shown is not to scale since $h \gg l$ (see Sec. V C). Harmonic motion about the trap center generates an alternating electric field which drives the mechanical flexure mode of the beam (light blue) via the piezoelectric effect. The ion position $r_{1,\text{opt}}$ maximizes the coupling and is close to but smaller than the beam length l , due to edge effects.

(see Fig. 7). Moreover, the dependence on time and spatial coordinates can be separated, i.e., $\vec{u}(r_1, t) = a(t)\vec{s}(r_1)$, where $\vec{s}(r_1) = (0, 0, s_3(r_1))$ is the mode shape (unitless) and $a(t)$ is its amplitude. The acoustic oscillation can therefore be reduced to a one-dimensional harmonic oscillator $a(t)$ with frequency ω_0 , effective mode mass M , and effective spring constant K as

$$M\ddot{a} = -Ka, \quad (18a)$$

$$M = \rho \int_V d^3r |s|^2, \quad (18b)$$

$$K = E \int_V d^3r \left| \frac{ds}{dr_1} \right|^2, \quad (18c)$$

where ρ is the material density, V is the volume of the beam, and E is its Young's modulus.

The harmonic motion of the ion can couple to the beam acoustic mode via piezoelectricity. A simplified model of the beam piezoelectric material is that of an ionic lattice. When the beam is at rest, the electric fields generated by the positive and negative charges inside it ideally cancel each other. If, however the ions are displaced from equilibrium nonuniformly,¹ the beam will exhibit a bulk polarization P that can interact with the electric field of the ion. Such a polarization therefore, depends linearly on the strain tensor composed of all the partial derivatives of the displacement components $\partial_i u_j \equiv \partial u_j / \partial r_i$ for $i, j \in \{1, 2, 3\}$. Since the strain tensor is symmetric, this linear relation can be written as $\vec{P} = e u'$ where e is the 3×6 matrix of piezo coefficients (in units of C/m^2) and u' represents strain in Voigt notation $u' = (\partial_1 u_1, \partial_2 u_2, \partial_3 u_3, \partial_2 u_3 + \partial_3 u_2, \partial_3 u_1 + \partial_1 u_3, \partial_1 u_2 + \partial_2 u_1)$. This bulk polarization will in turn be influenced by the ion electric field \vec{E}_{ion} . The coupling constant between the ion motion along the i th axis and the

¹A uniform displacement of all the ions cannot generate bulk polarization.

piezoelectric beam is

$$g_i = \frac{\int_V d^3r \partial_i \vec{E}_{\text{ion}} e s'}{2\omega_0 \sqrt{M m_{\text{ion}}}}, \quad i = 1, 2, 3. \quad (19)$$

Here we used the assumption that $\vec{u} = a(t)\vec{s}(r_1)$ and s' is defined in the same manner as u' .

The expression in Eq. (19) is general and not particular to any specific beam geometry. While the denominator is the standard term we encountered for two coupled mechanical oscillators [see Eq. (6)], the numerator is a rather involved overlap integral. To appreciate its complexity, we write its integrand in explicit matrix form as

$$\partial_i (E_{\text{ion},1}, E_{\text{ion},2}, E_{\text{ion},3}) \begin{pmatrix} e_{1,1} & \cdots & e_{1,6} \\ \vdots & & \vdots \\ e_{3,1} & \cdots & e_{3,6} \end{pmatrix} \begin{pmatrix} \partial_1 s_1 \\ \partial_2 s_2 \\ \partial_3 s_3 \\ \partial_2 s_3 + \partial_3 s_2 \\ \partial_3 s_1 + \partial_1 s_3 \\ \partial_1 s_2 + \partial_2 s_1 \end{pmatrix}. \quad (20)$$

This integrand can be understood as a dipole-dipole energy density. To see this, notice that since the field of the ion is that of a monopole, its spatial derivative $\partial_i \vec{E}_{\text{ion}}$ is equivalent to a dipole field aligned along the i th axis \hat{i} . We may therefore rewrite Eqs. (19) and (20) in terms of an integral over an effective dipole-dipole interaction as

$$g_i = \frac{1}{4\pi\hbar\bar{\epsilon}} \int_V d^3r \frac{3(\vec{p}_{\text{ion}} \cdot \hat{r})(\vec{P} \cdot \hat{r}) - \vec{p}_{\text{ion}} \cdot \vec{P}}{r^3}, \quad (21)$$

where

$$\vec{p}_{\text{ion}} = q \sqrt{\frac{\hbar}{2m_{\text{ion}}\omega_0}} \hat{i}, \quad (22a)$$

$$\vec{P} = e s' \sqrt{\frac{\hbar}{2M\omega_0}}, \quad (22b)$$

and we use $\bar{\epsilon} = (\epsilon_0 + \epsilon_{\text{dielectric}})/2$ since the field of the ion inside the piezoelectric material can be approximated as that of an ion in vacuum, with the dielectric constant of vacuum ϵ_0 replaced by $\bar{\epsilon}$, the average of the vacuum and dielectric constants [54].

A priori, the overlap integral in the numerator of Eq. (19) should not be expected to be large. The piezoelectric coefficient matrix e is a material property, while the mode shape \vec{s} is a result of both geometry and material constraints. Those impose a polarization density \vec{P} which need not necessarily align with \vec{p}_{ion} . We next perform a calculation for two specific piezoelectric resonators in order to demonstrate this difficulty. We use Eqs. (19) and (21) interchangeably.

C. Ion coupled to GaN nanobeam

Figure 8 shows an image of gallium nitride (GaN) nanobeams. A single beam, clamped at one end, can resonate in a flexure mode [55] with a resonance frequency of $\omega_0 = (\beta a^2 E / \rho l^4)^{1/2}$. Here, a is the cross-section radius, l is the beam length, E is its Young's modulus, ρ is its density, and β

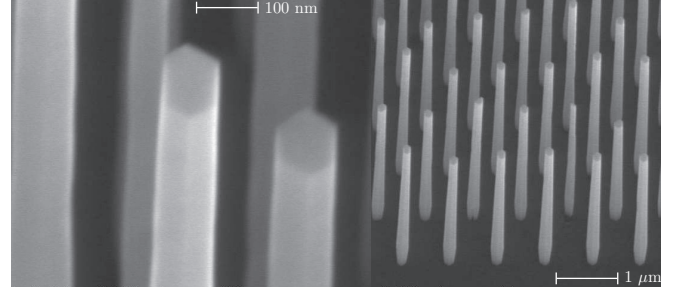


FIG. 8. SEM microscopy of GaN nanobeams with hexagonal cross section. Gallium nitride nanobeam photographs courtesy of K. Bertness, NIST, Boulder, Colorado 80305, USA.

is a numerical factor (3.09 for a circular cross section, 2.57 for a hexagonal cross section²).

We can estimate an upper limit on the coupling rate based on Eq. (19) and by using the simplified geometry in Fig. 7:

$$g = \frac{q\bar{\epsilon}A}{4\pi\bar{\epsilon}\hbar^3\omega_0\sqrt{Mm_{\text{ion}}}} f(h/l), \quad (23)$$

where f is a unitless geometric factor depending on the h/l aspect ratio, A is the cross-section area, $\bar{\epsilon}$ is the largest element of the 3×6 GaN piezo-coefficient matrix, and $\bar{\epsilon}$ is the average of its dielectric constant and that of vacuum. The ion position along the beam $r_{1,\text{opt}}$ is chosen so as to maximize the coupling. It turns out that $r_{1,\text{opt}} \sim 0.6l$ due to edge effects.

Figure 9 shows the coupling coefficient as a function of ion height h . At an experimentally attainable height of $h = 50 \mu\text{m}$, beam length $l = 15 \mu\text{m}$, and frequency $\omega_0 = 2\pi \times 868 \text{ kHz}$, the coupling strength is $g = 2\pi \times 235 \text{ Hz}$. Even for a beam with a relatively high quality factor of $Q = 6 \times 10^4$ [56], the product $gQ/2\pi = 1.4 \times 10^7 \text{ Hz}$ whereas the strong quantum regime requires $gQ/2\pi \gg 2.6 \times 10^{11} \text{ Hz}$ at 4 K and $gQ/2\pi \gg 3.3 \times 10^9 \text{ Hz}$ at 50 mK [Eq. (10)].

Based on Eq. (23), the coupling to materials other than GaN can be estimated. Another notable material is lithium niobate

²For a hexagon, the radius is defined to be that of the smallest circle enclosing it.

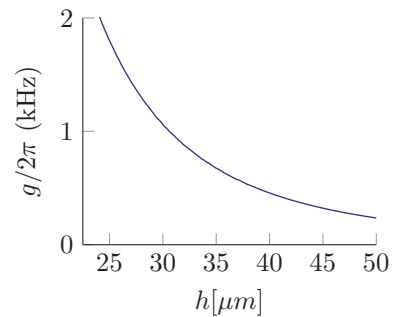


FIG. 9. Ion to GaN nanobeam piezoelectric coupling strength g vs ion height h above the beam. The beam cross section is as in Fig. 8. The geometry is as in Fig. 7 with $l = 15 \mu\text{m}$, $E = 3 \times 10^{11} \text{ kg m}^{-1} \text{ s}^{-2}$, $\rho = 6.15 \times 10^4 \text{ kg/m}^3$, $\bar{\epsilon} = 0.375 \text{ Cm}^{-2}$ (the strongest piezo coefficient of GaN), $\bar{\epsilon} = 5\epsilon_0$, with ϵ_0 being the vacuum permittivity. The beam flexure mode frequency is 868 kHz.

where the strongest of the piezoelectric coefficients is an order of a magnitude larger than for GaN, with the other parameters reasonably close to those of GaN [57]. That, however, would still have a gQ factor which is below our criteria ($N_{\text{osc}} \sim 10^{-4}$ at 4 K), and even that estimate assumes a high- Q lithium niobate resonator, which has yet to be demonstrated. Another approach would be to use beams with higher quality factors that are close to 10^6 ; for example, silicon nitride [58] doubly clamped beams or other resonators (see Tables 1 and 2 in Ref. [59]). However, since these resonators are not made from piezoelectric material, it would require incorporating piezoelectric material into the beam while maintaining the high quality factors.

D. Ion coupled to quartz resonator

Recent work with quartz bulk acoustic resonators at both 4 K and at temperatures of tens of millikelvin demonstrated quality factors of up to 7.8×10^9 and might therefore be useful as part of a hybrid quantum system [60–64]. Conveniently, the resonance frequencies of these devices are compatible with those of trapped ions, i.e., in the 5 to 15 MHz range.

A BVA resonator (Boîtier à Vieillessement Amélioré, enclosure with improved aging) is a quartz resonator designed for high- Q clock oscillators [65]. The resonator described here is formed from a disk of $L = 6.5$ mm radius and $t = 1$ mm thickness mechanically clamped at its rim (see Fig. 10). The mechanical motion of the disk is actuated by placing the disk between the two plates of a capacitor. The origin of the high- Q factors becomes apparent when considering the mechanical displacement profiles of one family of its acoustic modes [66]:

$$\vec{s}(x, y, z) = e^{-(x^2+z^2)/2\sigma^2} \sin(k_n y) \hat{y}. \quad (24)$$

Here an acoustic standing wave is formed along the unit vector $\hat{y} = (0.226, 0.968, 0.111)$ which is approximately along the \hat{y} axis (see Fig. 11). The mode k vector satisfies $k_n t = n\pi$, $n = 3, 5, \dots$ and has a radial Gaussian profile, with $\sigma \sim 1$ mm $< L$. This is very similar to the standing wave formed in a Fabry–Pérot optical cavity. The acoustic mode is therefore well protected from dissipation through contacts at the rim, where the disk is clamped. Other acoustic-mode families are not considered here since they exhibit lower quality factors [62]. This is also the reason why we do not consider the fundamental $n = 1$ mode of Eq. (24).

An ion can be coupled to the quartz resonator by trapping it a distance $h = 50$ μm from the surface, as shown in Fig. 11. Calculating the coupling strength can be accomplished by using Eq. (19) and considering the acoustic-mode shape [see Eq. (24)]. An upper bound, which does not take into account the relative angle between the derivative of the field of the ion and the polarization of the bulk, yields $g \sim 2\pi \times 1$ kHz. This is calculated by applying the Cauchy–Schwarz inequality to the integrand in Eq. (20) of the overlap integral in Eq. (19). When combined with the high quality factors involved ($Q \sim 10^9$), this yields $gQ/2\pi \sim 10^{12}$ Hz.

This bound, however, cannot be saturated when using the actual integrand in Eq. (20). To see this, recall Eq. (21) where g is expressed as an integral over the dipole-dipole interaction between the dipole defined by the ion motion, \vec{p}_{ion} , and the piezoelectrically induced polarization density \vec{P} . Figure 12

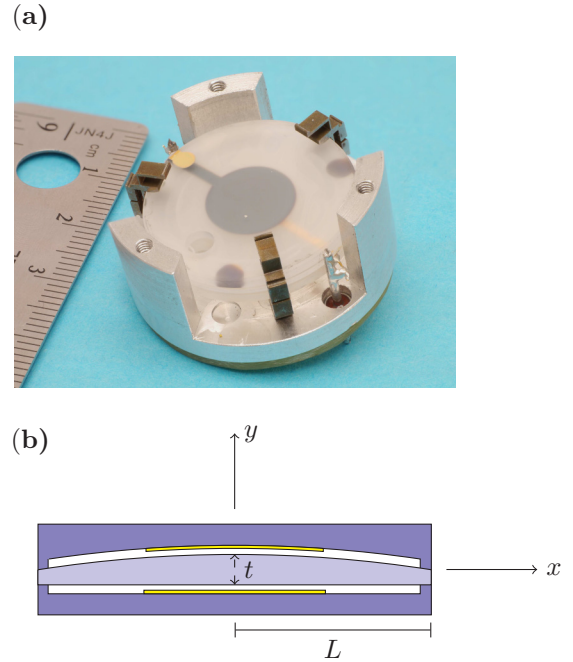


FIG. 10. High- Q quartz bulk acoustic resonator. (a) Photograph of a resonator. Device courtesy of Serge Galliou, FEMTO-ST institute, 25000 Besançon, France. (b) Schematic cross section. Quartz resonator of thickness t is shown by the light blue fill. Quartz holders (dark blue fill) clamp the resonator at its rim. The resonator is sandwiched between two metallic electrodes forming the actuating capacitor (yellow fill). Thickness of the electrodes as well as the gaps between the quartz resonator and the quartz holders are exaggerated for clarity. The modes with highest Q factor can be described by standing waves, approximately along the y axis, with resonant frequencies of $f_n \approx n \frac{v_s}{2t} = n \times 3.38$ MHz where $v_s = 6757$ m/s is the speed of sound and n is the mode number.

illustrates the structure of \vec{P} . Naturally its magnitude follows that of the acoustic mode, having a Gaussian radial profile and forming a standing wave along the \hat{y} axis. The polarization direction of each standing-wave antinode is approximately constant and opposite to that of its neighboring antinodes. Based on this structure, we can refine our upper bound for g

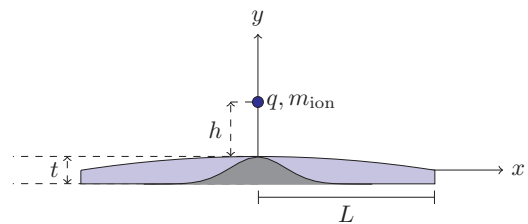


FIG. 11. Basic geometry for ion-to-quartz resonator coupling. An ion of mass m_{ion} and charge q is hovering at a distance $h = 50$ μm (exaggerated) above a disk of radius $L = 6.5$ mm and thickness $t = 1$ mm. The Gaussian radial profile of the acoustic mode is shown in gray. The ion motion generates an oscillating electric field that actuates the acoustic modes via piezoelectricity.

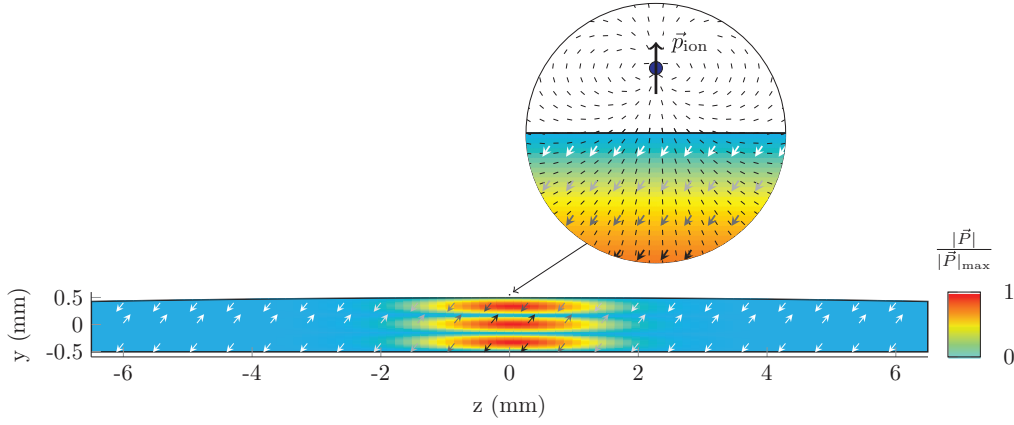


FIG. 12. Piezoelectrically induced polarization density \vec{P} for third-overtone acoustic mode [Eq. (24) with $n = 3$]. Magnitude (relative) is shown by the color plot. Direction is shown by the unit-vector arrows (darker arrows indicate stronger field strengths). Inset shows mode overlap between the electric-dipole field due to a fixed dipole \vec{p}_{ion} at the ion position, which is associated with its motion along \hat{y} , and the quartz resonator polarization density \vec{P} . The ion is assumed to be trapped $50 \mu\text{m}$ above the resonator surface. The integral over the dipole-dipole interaction between \vec{p}_{ion} and \vec{P} [Eq. (21)] yields a coupling strength $g/2\pi \leq 1 \text{ Hz}$ (see Appendix A).

by using

$$g \leq \frac{2|\vec{p}_{\text{ion}}||\vec{P}_{\text{max}}|}{4\pi\hbar\epsilon} \int_V \frac{d^3r}{r^3} \approx 3.2 \frac{|\vec{p}_{\text{ion}}||\vec{P}_{\text{max}}|}{4\pi\hbar\epsilon}, \quad (25)$$

where we utilized the fact that the interaction energy between two dipoles obtains a maximum when they are aligned with the vector \vec{r} connecting them. For the mode configuration in Fig. 12, we get $g \leq 2\pi \times 1.7 \text{ Hz}$. This bound is confirmed in Appendix A, where we numerically calculate the coupling strengths for various ion motion axes according to Eq. (19) and get $g/2\pi$ in the range of 0.49 to 1.46 Hz.

To increase the coupling strength, we could reshape the dipole field associated with the trapped ion to better match the acoustic-mode polarization density. A simple and practical way to do this is to use a capacitor to mediate the electric fields between the ion and the quartz resonator (see Ref. [15], Appendix C), as in Fig. 13. Here, the ion motion generates image currents on the trap electrodes that generate a time-varying, but uniform, electric field near the center of the crystal.

The coupling g can be calculated directly as done in Eq. (A 3). However, since the BVD equivalent capacitance C_{quartz} and inductance L_{quartz} of the quartz resonator have been measured for various acoustic modes, we present here a simpler analysis based on the BVD equivalent circuit of both the ion and the quartz resonator, shown in Fig. 13(b). We rewrite Eq. (9) for this case as

$$g = \frac{\omega_0}{2} \frac{\sqrt{C_{\text{ion}}C_{\text{quartz}}}}{C_{\text{trap}} + C_{\text{shunt}}}, \quad (26)$$

where we utilized the fact that the trap and shunt capacitances are much larger than the mechanical equivalent capacitances C_{ion} and C_{quartz} . In fact, $C_{\text{ion}} < 0.2 \text{ aF}$ [see Eq. (13)] and typical values for C_{quartz} are in the 1 to 200 aF range [67,68]. Therefore, it is imperative that the sum of the trap and shunt capacitance $C_{\text{total}} \equiv C_{\text{trap}} + C_{\text{shunt}}$ are kept to a minimum. On the other hand, the quartz capacitor must be large enough to have considerable overlap with the quartz acoustic mode. Because the mode radius is on the order of $\sigma \sim 1 \text{ mm}$, the

capacitor plate area should have a comparable radius, leading to $C_{\text{shunt}} \sim 0.13 \text{ pF}$, given the dielectric constant of these crystals $\epsilon = 4 \times 10^{-11} \text{ F/m}$. The trap capacitance, therefore, should be comparable or lower than that value. Figure 13(c) shows an ion-trap design where these low capacitances can be realized. The crux of the design is that, instead of forming a trap capacitor separate from the quartz resonator capacitor and connecting them with wires, the top capacitor plate of the BVA also serves as the trap bottom dc plate. This arrangement is therefore able to minimize the effect of additional stray capacitances. By using an electrostatic simulation, we estimate $C_{\text{total}} = 0.18 \text{ pF}$.

The capacitor reshaping of the ion electric field indeed improves the coupling to 10 to 20 Hz for known parameters of C_{quartz} . With N ions we get $gQ/2\pi \sim \sqrt{N} \times 10^{10} \text{ Hz}$, requiring a Wigner crystal of more than 100 ions in order to satisfy the strong-coupling regime constraint at 4 K. Maintaining such a crystal in the trap might not be trivial due to the anharmonicities and finite size of the trap. In Appendix A, we show that the coupling dependence on different device parameters and mode overtone number does not allow for substantial increases in g . It has been shown that high-overtone modes, e.g., $n = 65$, can exhibit quality factors of almost $Q \sim 10^{10}$ [62]. That high Q is counteracted by the $n^{-0.5}$ dependence of g in the mode number (see Appendix A).

Nonetheless, it is worth noting the outstanding properties of such a device. The mechanical mode, which is resonantly coupled to the ion motion, can potentially be cooled to near its ground state by laser cooling the ion. Since laser cooling can be done much faster than the coupling rate, the quartz cooling rate is close to $2g/2\pi$. The thermal heating rate is $(1 - e^{-1})n_{\text{thermal}}\tau_{\text{thermal}}^{-1} \approx (1 - e^{-1})k_B T/(\hbar Q)$ (see Sec. III). The steady-state number of quanta of the quartz acoustic mode would therefore be

$$\bar{n} \approx \pi(1 - e^{-1}) \frac{k_B T}{\hbar g Q}. \quad (27)$$

If operated at 4 K, the 5 to 15 MHz mechanical modes of the quartz resonator could be cooled to $\bar{n} \sim 16$ quanta by

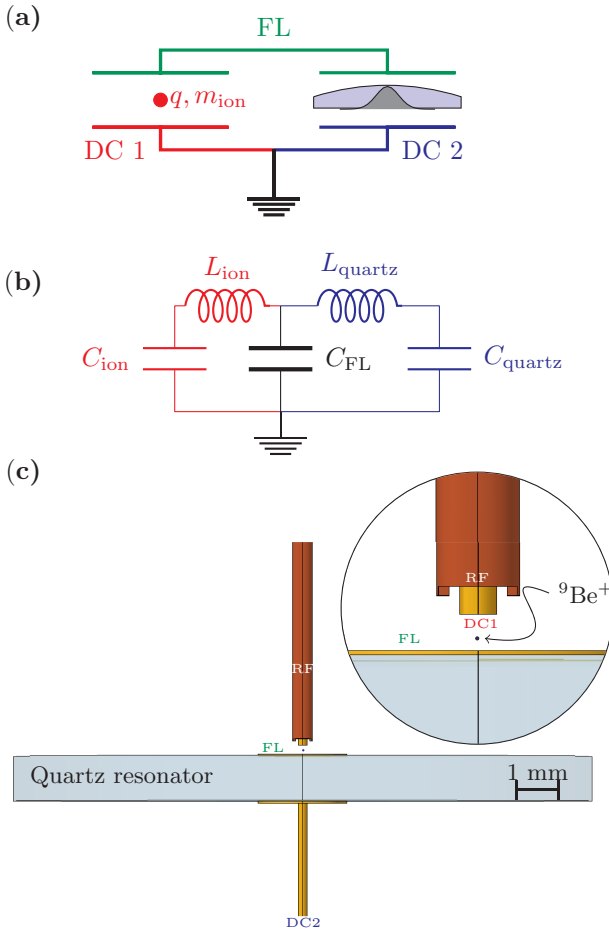


FIG. 13. Coupling an ion to a quartz resonator mediated by a shunt capacitor. (a) The ion is trapped between two endcap electrodes forming a capacitor between FL and DC 1. Ion motion generates image currents in the wires connecting the trap endcap DC1 and the quartz shunt capacitor (formed between FL and DC 2), which in turn generate an oscillating electric field at the quartz resonator, actuating its acoustic modes through piezoelectricity. (b) BVD equivalent circuit of the two coupled systems. The capacitance C_{FL} is the total capacitance between FL and ground. (c) A Paul trap design minimizing C_{FL} for maximal coupling of a ${}^9\text{Be}^+$ ion to the quartz resonator. The trap is formed from a circular inner dc electrode (DC 1), surrounded by an outer cylindrical shell rf electrode (RF). Two disks of 1 mm radius placed at the top (FL) and bottom (DC 2) of the quartz resonator form the quartz shunt capacitance. Ideally, the top plate should be kept floating (FL) or connected to ground by a large ($>G\Omega$) resistor. The trap drive circuitry that connects to the RF electrode and the RF ground connection between DC 1 and DC 2 is omitted.

laser cooling the coupled ion. Starting at dilution-refrigerator temperatures (<50 mK) would result in $\bar{n} \sim 0.2$ quanta. The mechanical coherence times $\tau_{\text{coh}} = \hbar Q/k_B T$ could reach ~ 2 ms in a 4 K environment and up to 150 ms in a 50 mK environment. Due to its very large mode mass (1 to 10 mg), such a device, if placed in a superposition state of motion, could be used to restrict certain decoherence theories of massive objects (see Sec. VII).

VI. PRACTICAL CONSIDERATIONS FOR COUPLING AN ELECTRON TO A SUPERCONDUCTING RESONATOR

In Sec. IV, we concluded that, based on its small mass, the electron is potentially the most favorable candidate for a strongly coupled hybrid system composed of a charged particle and a superconducting resonator. Coupling strengths on the order of 0.1 to 1 MHz can be expected for an electron trapped 50 to 100 μm away from the trap electrodes, requiring a very moderate quality factor of $Q \geq 10^4$ for the electrical resonator, at dilution-refrigerator temperatures. To estimate electron motional decoherence, we take the measured heating rates for trapped ions and extrapolate them to an electron with a secular oscillation frequency of 1 GHz. We find a heating rate of $\dot{n} \sim 100$ quanta/s, well below the coupling rate (see Appendix B).

An electron-based hybrid system might enable a fast and coherent quantum information processing technology. A platform of trapped electrons could be realized where the electron spin serves as the quantum bit (qubit). Unitary single and two-qubit gates can be implemented using rf gradients [69,70]. In the presence of magnetic gradients, the electron spin couples to its motion, which in turn is coupled to the underlying LC resonator. Spin initialization and readout could therefore be implemented with the superconducting resonator acting both as a reservoir and as an interface for readout circuitry (e.g., see Ref. [71]). The proposed architecture may be more scalable compared with trapped ion QIP since the interconnecting elements are chip based, requiring only rf or microwave control and no optical elements or laser beams. The absence of optical design constraints could allow for smaller traps, which translates into stronger coupling between electrons and superconducting elements, enabling faster two-qubit gates. Moreover, recent advances in QIP with trapped ions have reached gate speeds that are only an order of magnitude slower than the trap frequency [9]. If that scaling holds for electrons, that would correspond to tens of nanosecond gate times, making them on par with superconducting qubit gate times (see, for example, Ref. [72]). Qubit (i.e., spin) coherence could extend to seconds [73]. Therefore, an electron-based QIP platform could allow for a coherence time to gate time ratio of $\geq 10^8$, far exceeding any other QIP technology. Moreover, if the motional heating rates estimated in Appendix B are experimentally verified, such fast gates would correspond to a Bell-state generation fidelity error of $\sim 10^{-6}$ (see Ref. [74]).

The hybrid nature of such a system might offer an additional way, albeit slower, to entangle electrons, using the coupling to the underlying circuitry. This would enrich the QIP toolbox available for electron spins, for example, by entangling electrons in different traps that are far apart. Here, by using magnetic-field gradients, the spin of the electron can be entangled with its motion. Since the motion of each electron is strongly coupled ($g/2\pi \sim 0.1$ to 1 MHz) to a corresponding LC resonator, entanglement can be achieved by electrical coupling (either inductive or capacitive) of the two LC circuits. Moreover, the inclusion of Josephson-junction-based (JJ-based) devices could play an important role within the rf circuitry, allowing for greater flexibility in addressing and connecting electrons, e.g., by enabling tunable and/or parametric coupling [75,76] between electrons.

In addition, the electron could couple to an on-chip JJ-based qubit, a nonlinear resource with a high speed of operation. For example, swapping information to a JJ qubit could enable high-fidelity state readout (e.g., see Ref. [77]).

The idea of using trapped electrons as part of a hybrid quantum system was first suggested for Penning traps [15,29]. To that end, novel planar Penning traps have been developed and demonstrated [78,79]. Moreover, electrons were trapped with cryogenic planar Penning traps [80]. Although single electrons have already been detected in three-dimensional Penning traps by driving their motion [16,81], the anharmonicity of planar traps makes single-electron detection challenging. An optimization of the design of the planar trap electrodes [82] led to the detection of one or two electrons [83]. The outlook for planar Penning traps is discussed elsewhere [83–85].

Recently, an ensemble of $\sim 10^5$ electrons trapped on superfluid Helium with normal-mode frequencies in the tens of gigahertz range were nonresonantly coupled to a superconducting resonator at ~ 5 GHz [86]. By measuring dispersive shifts in the resonator frequency in the presence of the electrons, the authors could deduce a coupling strength of ~ 1 MHz per electron. Further studies of that technology could determine if the single-electron regime can be achieved, establishing a new and interesting route for quantum information processing with electrons, as proposed in Refs. [30,87–90].

The potential advantages and prospects of using rf Paul traps for electron-based quantum information processing were suggested and analyzed [18]. Clearly, since a Paul trap does not involve the strong magnetic fields required in a Penning trap, it naturally avoids exceeding the typical critical magnetic fields of superconducting circuitry. Strontium ions, for example, have been trapped with a superconducting niobium planar-chip trap [91]. Two-dimensional trapping of electrons with rf fields was recently demonstrated, resulting in guiding electrons along a given trajectory [92]. To date, however, electrons have been almost exclusively trapped in three-dimensional Penning traps, with the exception of Ref. [93]. There, a macroscopic combined Penning and Paul trap was used to simultaneously trap tens of ions and electrons.

In Ref. [18], a ring Paul trap design for electrons is analyzed, where a parametric coupling scheme is suggested, based on geometric nonlinearities of the potential. The coupling rates and decoherence rates reported here are consistent with those results. The trap volume used in Ref. [18] was relatively small [$5 \mu\text{m} \times \pi \times (15 \mu\text{m})^2$] with a trap depth of 1 meV, placing the electron $5 \mu\text{m}$ away from the nearest electrode, rendering a strong coupling of $g = 2\pi \times 1.1$ MHz.

Here, we analyze the experimental conditions of two trap geometries, aimed at achieving the strong-coupling regime, for a larger trapping volume and a deeper trap. As will be apparent in what follows, the design of these traps involves a delicate interplay between the trap stability and depth, its ability to maintain superconductivity, the energy range of the electron source, and the strong-coupling requirement. In broad strokes, it is easier to build a large trap that is stable and deep so that currently available electron sources could be used. Large trap dimensions, however, would prevent satisfying the coupling criteria in Eq. (10). On the other hand, a small trap is optimal for strong coupling, but it can only support a shallow trapping potential and therefore requires a low-energy electron source to

ensure trapping. Because these problems are intertwined, our presentation includes a discussion of each of these aspects, as well as their compatibility.

A. Stable trapping of electrons

A Paul trap [1] is formed when a time-varying voltage $V_{\text{rf}} \cos(\Omega_{\text{rf}} t)$ is applied to an electrode arrangement that gives a quadratic spatial dependence for the electric potential in the neighborhood of its electric-field null point. For simplicity, we assume cylindrical symmetry and write the time-varying potential in terms of the standard (ρ, z) cylindrical coordinates as

$$\begin{aligned} \phi &= q V_{\text{rf}} \cos(\Omega_{\text{rf}} t) \Phi(\rho, z), \\ \Phi(\rho, z) &= \beta \frac{\rho^2 - 2z^2}{d^2} \text{ for } \rho, z \ll d, \end{aligned} \quad (28)$$

where q is the electron charge, β is a unitless geometry prefactor ($\beta = 1$ for an ideal quadrupole), and d is the trap electrodes' length scale (e.g., distance from the trap center to the nearest point of an electrode surface). The time-varying field generates a confining potential provided that the Mathieu criterion for stability is satisfied [1]:

$$q_{\text{mathieu}} \equiv \frac{8\beta q V_{\text{rf}}}{m d^2 \Omega_{\text{rf}}^2} < 1. \quad (29)$$

The confinement can then be described, to lowest order, by a time-independent pseudopotential:

$$\phi_{\text{pseudo}} = \frac{q^2 V_{\text{rf}}^2}{4m \Omega_{\text{rf}}^2} |\nabla \Phi|^2, \quad (30)$$

where m is the electron mass. It follows that the pseudopotential trap depth can be expressed as $D = q V_{\text{rf}} q_{\text{mathieu}} / \zeta$, where ζ is a unitless factor dependent only on the trap geometry. For a perfect quadrupole trap $D = q V_{\text{rf}} q_{\text{mathieu}} / 6$, whereas, for example, for a planar “five-wire” surface electrode trap [94], $D = q V_{\text{rf}} q_{\text{mathieu}} / 404$.

The first constraint we consider is trap stability [Eq. (29)]. Since the electron mass is small compared with ions, either the trap voltage should be lowered or the trap scale d and/or frequency Ω_{rf} should be increased, as compared with ion traps, to maintain stability. Lowering the voltage would reduce the trap depth and increasing d would diminish the coupling strength. Therefore, it appears to be advantageous to increase the trap frequency to the gigahertz regime.

The second parameter we consider is trap depth. Naturally, it is easier to trap electrons in a deeper trap. For that purpose, increasing V_{rf} is beneficial. Other constraints; namely, the need to maintain superconductivity in the trap electrodes and circuitry, limit the maximal rf voltage to a few tens of volts (see Sec. VIB). Thus far, the shallowest Penning trap that was able to maintain trapped electrons had a trap depth of $D \sim 1$ eV, the electrons being loaded first into a 5-eV-deep trap whose voltages were subsequently lowered to form the 1 eV trap [83]. We therefore require the trap depth to be at least $D \sim 1$ eV.

Figure 14 shows two different three-dimensional geometries of traps satisfying the above constraints. Table II

TABLE II. Trap parameters for the designs shown in Fig. 14. The pseudopotential secular frequencies are ω_x , ω_y , and ω_z where x , y are in the plane of the rf ring and z is perpendicular to it, D is the trap depth, C_{trap} [see Eq. (14)] is the inherent total capacitance between the dc endcaps and g is the electron-superconducting resonator coupling rate [see Eq. (14) as well as Fig. 17 for circuit schematics]. With the above choices of d , the geometric parameter in Eq. (14) is $\alpha \sim 1$ for both traps. Parameters are estimated by using an electrostatic simulation (this is a reasonable approximation since in both traps the rf wavelength is >10 cm, i.e., much larger than trap dimensions). The maximal rf current I_{rf} is estimated based on $I_{\text{rf}} = \Omega_{\text{rf}} C_{\text{trap}} V_{\text{rf}}$. Additional capacitance would result in higher values for the rf current.

Parameter	Fig. 14(a)	Fig. 14(b)
V_{rf}	50 V	50 V
I_{rf}	42 mA	243 mA
$\Omega_{\text{rf}}/2\pi$	9 GHz	7.15 GHz
$\omega_x/2\pi$	0.6 GHz	0.75 GHz
$\omega_y/2\pi$	0.6 GHz	0.75 GHz
$\omega_z/2\pi$	1.2 GHz	1.5 GHz
D	1 eV	0.9 eV
q_{mathieu}	0.4	0.6
C_{trap}	15 fF	108 fF
d	100 μm	200 μm
g	$2\pi \times 1.2$ MHz	$2\pi \times 203$ kHz

summarizes the resulting trap parameters. Figure 14(a) describes a three-dimensional configuration of electrodes similar to that of Ref. [95]. Here, the trap endcap-to-endcap distance is set to $d = 100 \mu\text{m}$ in order to yield reasonable coupling, while keeping a minimum distance of $50 \mu\text{m}$ between the ion and the nearest electrode to avoid large heating rates. The coupling also

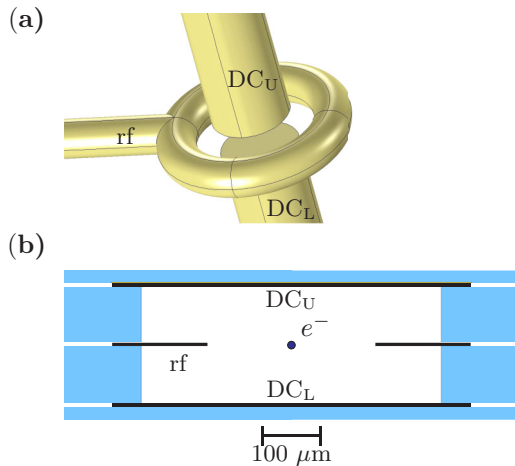


FIG. 14. Two Paul trap designs for electron trapping. (a) An rf ring with $300 \mu\text{m}$ inner diameter and $500 \mu\text{m}$ outer diameter forms a quadrupole field at its center with respect to two dc endcaps. The flat-ended endcaps have a diameter of $200 \mu\text{m}$ and are $100 \mu\text{m}$ apart. (b) A two-dimensional cut through a stacked chip version of (a). The blue region is a silicon substrate. The electron is trapped at the center of the middle rf ring electrode. The upper and lower endcap disks are $200 \mu\text{m}$ apart. The center ring inner diameter is $240 \mu\text{m}$ and the silicon-free region diameter is $500 \mu\text{m}$. Table II summarizes the resulting trap parameters.

benefits from having no nearby dielectrics, thereby minimizing the trap capacitance. The challenge in constructing such a trap, however, is the tolerance required for holding and aligning the electrodes. One way to solve this is shown in Fig. 14(b) where a trap is constructed from stacked chips, with lithographically patterned metal electrodes, pressed and aligned together [96,97]. Because convenient wafer thickness is $\geq 100 \mu\text{m}$, $d = 200 \mu\text{m}$ and the trap capacitance is increased (due to the additional dielectrics), lowering the coupling rates.

B. Maintaining superconductivity

An immediate concern with the above designs is that the relatively high rf currents involved will generate dissipation and magnetic fields that could potentially lead to breakdown of the superconductivity in the trap electrodes. Usually, the electrodes of Paul traps form part of the capacitance C of a parallel rf LC resonator (e.g., in Fig. 17, it would be the total capacitance between the two leads of L_{rf}). We can estimate the on-resonance peak current I_{max} from the rf voltage amplitude V_{rf} by using $\frac{1}{2} L I_{\text{max}}^2 = \frac{1}{2} C V_{\text{rf}}^2$. We find I_{max} in the range of 200 to 400 mA for the conditions described below.

For simplicity, we restrict our analysis to thin film wires on chip, where an analytic treatment is available. The critical current I_c , above which a thin film wire is no longer superconducting, is

$$I_c = \frac{\Lambda \sqrt{wb}}{0.74} J_c, \quad (31)$$

where b is the film thickness, w is its width, Λ is the London penetration depth of the superconducting material, and J_c is its critical current density [98].

Of the two commonly used materials for superconducting circuits; namely, aluminum (Al) and niobium (Nb), aluminum is disadvantageous due to its lower values for J_c and Λ and, with a critical temperature of $T_c = 1.2$ K, it requires operation at dilution-refrigerator temperatures. For example, a $100 \text{ nm} \times 10 \mu\text{m}$ aluminum wire has a critical current of $I_c = 11.3$ mA. A niobium wire with the same dimensions would have a critical current of $I_c = 221$ mA and would be fairly strongly superconducting even at 4 K ($T_c = 9.2$ K).

To maintain superconductivity in the chip-based design in Fig. 14(b) with niobium films, we require thicknesses and widths that satisfy $bw > 16 \mu\text{m}^2$. Here, the features of the narrowest electrode or wire would serve as the bottleneck determining the critical current for the entire circuit. For example, a $50 \mu\text{m} \times 500 \text{ nm}$ film cross section would be convenient to fabricate and could provide $I_c = 1.105$ A. These numbers are compatible with those measured in a superconducting niobium trap for strontium ions [91].

Equation (31) actually constrains the dc critical current through a wire; however, the rf critical current for a superconducting resonator has similar values [99], at least for the case of a half-wavelength stripline resonator. Whether a similar result holds for a lumped element resonator, where the current distribution is significantly different, has yet to be demonstrated.

C. Low-energy electron source

In principle, one method to load electrons into the trap would be to target the trapping volume with slow electrons and capture them by turning the trap on when they reach the trap center. In this case, the challenge lies in the fast electronics required. A slow electron source could be, for example, an ultracold GaAs photocathode [100,101], which has demonstrated beams with less than 1 eV average energy and less than 50 meV energy spread [102]. Such slow 0.1 to 1 eV electrons traversing a trap with a typical length of 100 to 200 μm requires turning the trap on faster than 0.1 to 1 ns. In Sec. VID, however, we show that the trap resonator quality factor should exceed 10^4 in order to comply with the typical cooling power of a cryogenic refrigerator. This would realistically limit the switching time of such a trap to the microsecond regime. We could mitigate this problem by constructing even slower electron sources. For example, using electron tunneling from bound states on the surface of liquid helium [103] could potentially generate <1 meV electrons, thereby relaxing the trap-switching-time constraint. The analysis of such a source is beyond the scope of this paper.

A second type of electron source, which is commonly used in Penning traps, is based on secondary electrons [104,105]. For example, in Ref. [83], a sharp tungsten tip was used to field emit high-energy (≥ 200 eV) electrons that collided with the trap surfaces, liberating gas molecules. During this process, some of these molecules reach the trapping region where they have a probability of being ionized by the incoming fast electrons. The relatively slow “secondary” electrons generated in the ionization process can then be trapped.

This approach seems to be effective with deep (≥ 5 eV) and large ($d = 0.1$ to 2 cm) traps [83]. Trap depth U_{depth} is defined as the maximum minus the minimum of the trap pseudopotential within the trap volume. It is not obvious that this technique would be efficient enough for a $U_{\text{depth}} = 1$ eV trap with a typical length scale of 100 μm . As an alternative, photo-ionization of a cold atomic gas could be more compatible with a shallow trap (e.g., see Ref. [106]), albeit at the expense of requiring optical access to the cryogenic chamber of the electron trap. One would also have to consider whether the cold atoms would immediately stick to the trap surfaces thereby creating a possible charging effect that would change the trapping potential. Here, we consider a refinement of the secondary electron technique that might be less violent to the trap electrodes, as well as increase the trapping probability, while not requiring optical access.

Rather than directing the incoming beam of electrons at the trap electrodes, we consider focusing the beam into the center of the trapping region and away from any surfaces. As a source of secondary electron emitters, a cold charcoal adsorber containing helium might be used. Primarily used for pumping residual helium gas, a charcoal adsorber can be heated with a resistor in order to liberate some helium and increase its vapor pressure in the chamber [107]. Incoming electrons will ionize the helium gas and generate secondary electrons that could then be trapped. In Sec. VID we show that, in order to accommodate for the heat load generated by the trap, it should be operated at temperatures in the range of 1 to 4 K

and not dilution-refrigerator temperatures. That would also leave enough cooling power to remove the heat generated by the charcoal heating resistor. We henceforth assume that the refrigerator is operated at 4 K.

The total cross section for helium ionization is maximal when the incoming electrons have a kinetic energy of $E_p \sim 120$ eV [108]. Here, however, we are interested in maximizing the cross section for generating low-energy secondary electrons rather than the total ionization cross section. In fact, since the threshold ionization for helium is ~ 24.58 eV, it is not surprising that the low-energy cross-section peaks at $E_p \sim 30$ eV [109,110]. The incoming electron energy should therefore be set to around 30 eV, resulting in an optimal cross section of $\sigma_{\text{ion}} \sim 0.05 \text{ \AA}^2$ for secondary electrons with energy below 1 eV [109]. The resulting ionizing rate of helium atoms within the trapping volume is

$$\Gamma_{\text{ion}} \simeq \frac{J \pi r_0^2}{q_e} n_{\text{He}} J \sigma_{\text{ion}}, \quad (32)$$

where J is the incoming current density of electrons, q_e is the electron charge, r_0 is the incoming electron beam radius, l is the radius of the spherical trapping volume, and n_{He} is the vapor density of helium atoms. We restrict the discussion to secondary electron generation due to the interaction of helium with the primary incoming electron beam. Additional ionization events due to, for example, elastically scattered electrons, could only increase Γ_{ion} . In the presence of the rf trap, the incoming electron energy E_p will be spread by less than ± 15 eV around 30 eV, as shown in Appendix C. This, in turn, could reduce the average value of σ_{ion} by $<18\%$ to $\sigma_{\text{ion}} > 0.041 \text{ \AA}^2$ (see Ref. [109]). Equation (32) can therefore be considered as an average estimate for Γ_{ion} . In addition, trap rf voltage can deflect the incoming electrons, causing the average beam radius to expand to $r_1 = \xi r_0$. Since the rf trap voltages V_{rf} considered in this paper have the same order of magnitude as E_p/q_e (see Table II), $\xi \leq 4$ as shown in Appendix C. We can still use r_0 in Eq. (32) since it depends on the total current of electrons traversing the trapping region. As long as $r_1 < l$, electrons are not lost due to collisions with the trap walls and this total current should be preserved.

The steady-state number of trapped electrons is determined by the ratio between the low-energy secondary electron generation rate Γ_{ion} and the total electron loss rate. Electrons that have already been trapped may collide with incoming electrons or with the surrounding helium atoms. The average energy of the electrons gradually increases due to these collisions (heating) until eventually it exceeds the trap depth and they are lost (boiling).

In Appendix C, we derive analytically an upper bound on the contribution to the heating rate due to collisions with incoming electrons. Briefly, since each collision is a Rutherford-type scattering problem, it cannot be attributed a finite cross section. Its geometric scale is therefore dictated by the incoming electron beam finite radius r where $r_0 \leq r \leq r_1$. Therefore, the average energy a single trapped electron gains in a single collision is $< q_e^2 / (4\pi \epsilon_0 r_0)$. Since the rate of collisions is $J \pi r_0^2 / q_e$ the resulting heating rate is $(dE/dt)|_e <$

$Jr_0q_e/(4\epsilon_0)$. This translates to an electron loss rate of

$$\Gamma_e = \frac{1}{U_{\text{depth}}} \left(\frac{dE}{dt} \right) \Big|_e < \frac{Jr_0q_e}{4\epsilon_0 U_{\text{depth}}}. \quad (33)$$

The contribution to the heating rate due to collisions with the helium gas is known as “rf-heating.” This follows from the helium atom playing the role of a hard immovable ball in the collision process, being much heavier than the electron. Therefore, when an electron collides with it, its instantaneous micromotion kinetic energy before the collision transforms into the secular motion energy after the collision [111,112]. During the harmonic secular motion of the ion, kinetic energy is exchanged between rf and secular motion, the rf fraction being maximal farthest from the trap center and ideally zero at the center. Therefore, collisions that occur farther from the center will potentially transfer more energy into the secular motion. If the secular energy of the trapped electron prior to collision is E_{in} , the energy gain after a single collision is $\leq E_{\text{in}}/2$, when averaging over the secular motion period. Assuming that the trapped electrons have a uniform energy distribution between 0 and U_{depth} , the average energy gain per collision with a single helium atom is less than $U_{\text{depth}}/4$. The rate of collisions in this case is $\sim \sigma_{\text{elastic}} n_{\text{He}} \langle |v| \rangle$ where $\sigma_{\text{elastic}} \sim 6 \text{ \AA}^2$ is the electron-helium elastic cross section for low-energy ($\leq 2 \text{ eV}$) electrons [113] and $\langle |v| \rangle \sim \frac{4\sqrt{2}}{3\pi} \sqrt{U_{\text{depth}}/m_e}$ is the average velocity of the trapped electrons, with m_e being the electron mass. The resulting heating rate is $(dE/dt)_{\text{He}} < \sigma_{\text{elastic}} n_{\text{He}} \langle |v| \rangle U_{\text{depth}}/4$. We translate it to an electron loss rate of

$$\Gamma_{\text{He}} < \frac{1}{U_{\text{depth}}} \left(\frac{dE}{dt} \right) \Big|_{\text{He}} = \frac{\sigma_{\text{elastic}} n_{\text{He}}}{3\pi} \sqrt{\frac{2U_{\text{depth}}}{m_e}}. \quad (34)$$

Combining Eqs. (32)–(34), the steady-state number of electrons in the trap, N_e , is dictated by setting $dN_e/dt = 0$ in the rate equation

$$\frac{dN_e}{dt} = \Gamma_{\text{ion}} - N_e(\Gamma_e + \Gamma_{\text{He}}). \quad (35)$$

For trapping, we require the steady-state number of electrons N_e be greater than a threshold value $N_{\text{threshold}}$, as we discuss below. This can always be satisfied if the current density J and the density of helium, n_{He} , are large enough [Eq. (35)]. To see this quantitatively, in Fig. 15(a), we plot the number of steady-state electrons for different current densities and helium-pressure values.

The value for $N_{\text{threshold}}$ depends on the dynamics of the electron loading process; specifically, on the cooling rate of the electron motion Γ_{cool} during loading. Without cooling, once the incoming electron source is turned off ($J \rightarrow 0$), any trapped electrons would rapidly boil out of the trap due to collisions with the helium background gas. Indeed, the helium pressure can be decreased significantly to avoid this process by allowing the charcoal adsorber to cool to its 4 K surroundings. However, the timescale for removing the helium is likely to be long compared with $1/\Gamma_{\text{He}}$. The latter is inversely proportional to the helium pressure and, for example, equals $1.3 \mu\text{s}$ at a helium pressure of 10^{-2} Pa . Collisions with other atoms are neglected in our discussion because we expect the trap

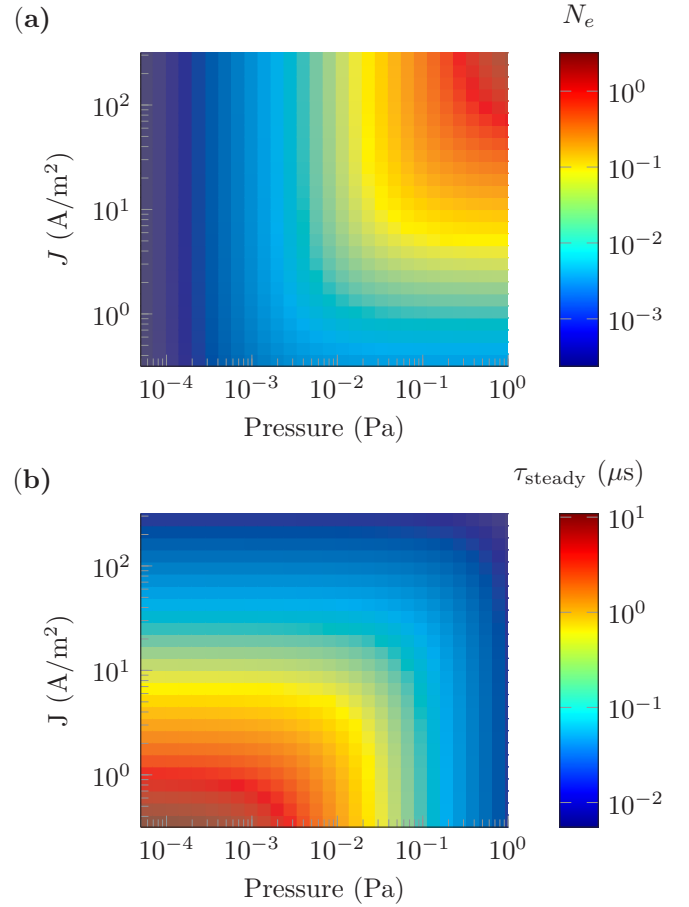


FIG. 15. Effect of loading parameters. (a) Estimated steady-state number electrons, N_e , in a 1-eV-deep trap having a trapping volume of $\sim(95 \mu\text{m})^3$ when the electron gun is on. Incoming electron beam radius is assumed to be $r_0 = 10 \mu\text{m}$. (b) $1/e$ time to reach steady-state number of electrons.

chamber to be in an ultrahigh vacuum cryogenic environment with pressures of 10^{-10} Pa or less.

In the design we consider below, we assume the z motion of the trapped electrons is strongly coupled to an LC resonator to experience damping. In Sec. VI E, we show that a $\sim 1 \text{ GHz}$ LC resonator with a quality factor $Q_{\text{det}} \sim 1000$ should suffice for single-electron detection. Therefore, the LC resonator equilibrates with its 4 K surroundings at a $\sim 1 \text{ MHz}$ rate, i.e., much faster than the coupling rate g between the LC resonator and the electron motion. The resulting z -motion damping rate is dictated by the slower of the rates, $\Gamma_{\text{cooling}} \sim g/2\pi \geq 100 \text{ kHz}$. To cool the x and y motion, these modes could be parametrically coupled to the z motion [114] as discussed in Sec. VI F. We will henceforth assume a similar damping rate for all axes.

Once the incoming electron beam is turned off, the trapped-electron energy E is dictated by the cooling rate and the helium collision-induced heating rate:

$$\frac{dE}{dt} = -\Gamma_{\text{cool}} E + \frac{1}{\pi} (\sigma_{\text{elastic}} n_{\text{He}}) \sqrt{\frac{2E}{m_e}} E. \quad (36)$$

For this equation to be correct, the initial energy of the electron must be below a value E_{init} determined by trap anharmonicity, which manifests as an amplitude dependence of the resonant frequency. Since damping is based on resonant coupling to the LC resonator, large-amplitude motion will not cool effectively. Based on Sec. VIE, we can estimate $E_{\text{init}} \lesssim 0.3$ meV. This threshold can be increased in a few ways. One technique could be to detune the trap in order to match the resonant frequency of higher-energy electrons, then adiabatically follow their frequency as they cool down. Another way is to design a trap with lower anharmonicity (see references in Sec. VIE). A third way could be to design an LC resonator with a tunable quality factor by using a tunable coupler [75,115] where the Q factor is first lowered for cooling purposes and increased once the electrons are cold. For the sake of the discussion here, we will adopt the more conservative estimate for E_{init} of ≤ 0.3 meV.

To achieve net cooling, the right-hand side of Eq. (36) should be negative, i.e.,

$$E \leq E_{\text{capture}} \equiv \frac{m_e}{2} \left(\frac{\pi \Gamma_{\text{cool}}}{\sigma_{\text{elastic}} n_{\text{He}}} \right)^2. \quad (37)$$

Therefore, if the electron z motion satisfies $E < E_{\text{thresh}} \equiv \min(E_{\text{capture}}, E_{\text{init}})$, it will remain trapped. For helium pressures below 0.027 Pa, E_{init} is the smaller of the two and determines $E_{\text{thresh}} = 0.3$ meV. For a pressure P greater than that, $E_{\text{thresh}} = E_{\text{capture}} = 0.3 \text{ meV} \times (0.027 \text{ Pa}/P)$.

Equation (36) was based on the assumption that excess micromotion can be neglected. Excess micromotion occurs when the ion experiences rf fields even at its equilibrium position that is usually shifted from the rf null due to stray fields. This would lead to a constant heating term in Eq. (36), thereby limiting both E_{capture} as well as the steady-state energy. By using dc compensation fields, the electron position can be adjusted back to the rf null. We require the heating rate due to excess micromotion to be much lower than the heating rate for electrons with E_{capture} energy. If the electron is at a position x away from the rf null, this constraint can be written as $m_e v_{\text{mm}}^2(x) \ll E_{\text{capture}}$ where $v_{\text{mm}}(x)$ is the micromotion velocity amplitude at x . For a 1 GHz trap and $E_{\text{capture}} = 0.3$ meV this constrains $x \ll 1 \mu\text{m}$.

From Figs. 15(a) and 15(b) we can extract the time needed to trap a single electron. Within the parameters explored, the steady-state number of trapped electrons, N_e , is less than one and the threshold energy is $E_{\text{thresh}} \sim 0.3$ meV or smaller. Therefore, the loading process should be operated in pulsed mode, with $\sim (U_{\text{depth}}/E_{\text{thresh}})/N_e$ pulses required on average to trap a single electron (provided that the electron energy distribution is uniform between zero and U_{depth}). Combined with the $1/e$ time required to reach the steady state [Fig. 15(b)], we extract the average total time required for trapping a single electron, shown in Fig. 16(a). As long as E_{thresh} is not dominated by the helium pressure P , i.e., by E_{capture} , increasing P is beneficial since N_e increases. An optimal helium pressure of ~ 0.027 Pa is reached, beyond which $E_{\text{thresh}} = E_{\text{capture}} \propto 1/P^2$.

These estimates assume that, once a single electron is trapped, it is immediately detected. Realistically, some sort of detection procedure needs to be applied in order to verify

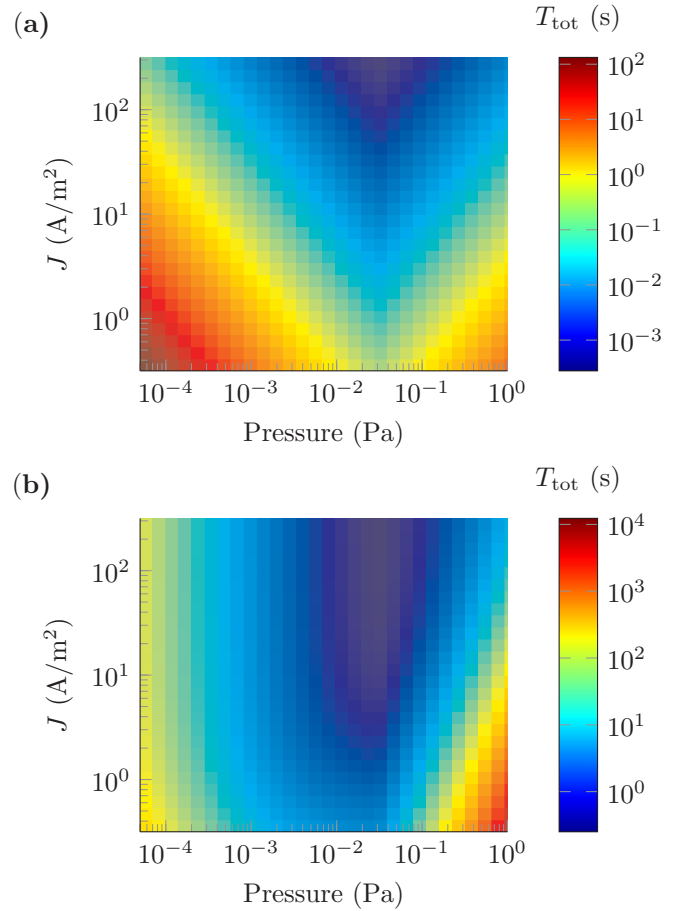


FIG. 16. Estimated average total time T_{tot} for trapping and detecting a single electron, based on the same parameters used for Fig. 15. The incoming electron beam gun is operated in pulse mode, the duration of each pulse [Fig. 15(b)] allows a steady-state number of electrons [Fig. 15(a)]. This translates into a probability of trapping a single electron after a single pulse. The process must be repeated a number of times, which is inversely proportional to that probability. After the electron loading pulse, a detection procedure needs to be applied for T_{det} . (a) Assuming $T_{\text{det}} = 0$, i.e., negligible. (b) Assuming $T_{\text{det}} = 10 \mu\text{s}$ based on the conservative detection-time estimates from Sec. VIE.

that indeed an electron is present. In Sec. VIE, we analyze the detection scheme of Ref. [31]. We estimate that the time to detect a single electron T_{det} is in the 1 to 10 μs range. In Fig. 16(b), we plot the total time required to trap and detect a single electron for the more conservative estimate of $T_{\text{det}} = 10 \mu\text{s}$. Based on the plot, working in the helium pressure range of 10^{-4} to 10^{-1} Pa and a current-density range of 1 to 100 A/m^2 , the range of times we get is similar to that of Paul trap loading times for ions.

The current-density range in Figs. 15 and 16 is chosen such that the total current of incoming electrons is in the nano-ampere regime for a beam radius of $r_0 = 10 \mu\text{m}$. The beam radius was chosen so that, even after expansion to r_1 due to the trap rf fields, it would avoid the trap walls. These parameters can be easily obtained with commercial electron sources. Smaller beam radii with the same total current would reduce the total time required to trap an electron even further.

That would require a design of electron optics combined with either a commercial or homemade cold field emission source, the details of which are beyond the scope of this paper.

D. Electrical circuitry

Stable trapping requires applying large voltages and currents in a cryogenic environment, next to a sensitive detection resonator. This has implications on the heat load experienced by the refrigerator and the circuit design of the trap.

Achieving a trap drive amplitude of $V_{\text{rf}} = 100$ V at frequencies in the 7 to 9 GHz range requires resonating the trap capacitance C_{rf} with an inductor. The resulting dissipation rate would be $P_{\text{dis}} = \Omega_{\text{rf}} C_{\text{rf}} V_{\text{rf}}^2 / Q$, where Q is the rf resonator quality factor. With $C_{\text{rf}} \leq 150$ fF (based on simulations of the traps in Fig. 14) and Q in the 10^4 to 10^5 range, implies ≤ 0.2 to 2 mW of dissipated power for frequencies in the 7 to 9 GHz range. With the cooling power of a dilution refrigerator typically being in the 100 to 400 μW range at $T = 100$ mK, too low to survive such heat loads, it seems that working at 4 K would be required, where 2 mW of power dissipation is easily absorbed, even with a lower ($Q \sim 10^4$) quality factor. In fact, even 1–2 K cryostats with ~ 60 to 200 mW of cooling power would suffice.

To understand the implications of the trap drive on the electron detection circuit, we model the traps in Figs. 14(a) and 14(b) with the lumped-element circuit shown in Fig. 17. Detecting the presence of electrons would be accomplished by using a tank circuit technique [31,81]. The electron thermal motion generates image currents that couple to the resonator formed from the trap capacitance and the inductor L_{det} , chosen to be resonant with the ~ 1 GHz secular motion. The trap is driven by a different resonator, formed from the ring-to-end-caps capacitance and another inductor, L_{rf} , chosen to resonate at the 7 to 9 GHz drive frequency.

The possible cross talk between the drive and detection resonators could deteriorate their respective quality factors. If the trap is electrically symmetric, i.e., $C_{\text{rf},1} = C_{\text{rf},2}$ and $C_{\text{iso},1} = C_{\text{iso},2}$, the two circuits are essentially orthogonal. The detection circuit is connected to equipotential points in the trap drive circuit and is therefore not influenced by the high currents flowing there. Moreover, due to the Wheatstone bridge topology, the detection circuit is not sensitive to the rf inductor L_{rf} and its coupling port. It is only influenced by the additional capacitances $C_{\text{iso},j}$ for $j = 1, 2$ that add to the total trap capacitance. Similarly, the rf resonator is indifferent to the added impedance of the detection resonator. The impact of trap asymmetry on the quality factor of the two resonators can be estimated by

$$\frac{\Delta Q_{\text{rf}}}{Q_{\text{rf}}} \sim \frac{Q_{\text{rf}} \omega_0}{Q_{\text{det}} \Omega_{\text{rf}}} \frac{C_{\text{cap}}}{C_{\text{iso},1} + C_{\text{rf},1} + 2C_{\text{cap}}} \epsilon, \quad (38a)$$

$$\frac{\Delta Q_{\text{det}}}{Q_{\text{det}}} \sim \frac{Q_{\text{det}} \omega_0}{Q_{\text{rf}} \Omega_{\text{rf}}} \frac{C_{\text{iso},1} + C_{\text{rf},1}}{C_{\text{iso},1} + C_{\text{rf},1} + 2C_{\text{cap}}} \epsilon, \quad (38b)$$

$$\epsilon = \frac{|C_{\text{rf},1} - C_{\text{rf},2}| + |C_{\text{iso},1} - C_{\text{iso},2}|}{C_{\text{rf},1} + C_{\text{iso},1}}, \quad (38c)$$

where Q_{rf} and Q_{det} are the rf and detection resonator quality factors, respectively, when the trap is completely symmetric, ΔQ_{rf} and ΔQ_{det} is their respective change due to asymmetry,

$\omega_0 \sim 2\pi \times 1$ GHz is the secular frequency, $\Omega_{\text{rf}}/(2\pi) \sim 7$ to 9 GHz is the trap drive frequency and ϵ is the asymmetry parameter. Clearly, if Q_{rf} and Q_{det} are comparable, and the capacitances involved are of the same order of magnitude, then keeping ϵ below a few percent should suffice.

E. Nonlinearity and detection of a single electron

One of the main concerns with detecting a single electron in Penning trap experiments is the trap anharmonicity [80,82,84]. In these traps, the signal of a single electron has a few-hertz linewidth due to damping resulting from its coupling to the detection circuit, whereas the effect of anharmonicity in these planar traps is to broaden the electron detection signal to 10 kHz to 1 MHz. However, in Ref. [82], it was shown that, by adding compensation electrodes and carefully adjusting their relative voltages, we could avoid the dominant anharmonic terms of the potential. Similarly, careful consideration for electrode shape and geometry allow for higher degree of harmonicity in three-dimensional traps [116,117].

In the designs considered here, the electron is strongly coupled to the detection circuit, giving a relatively broad signal linewidth, which in turn relaxes the constraints on the trap harmonicity. By assuming a moderate quality factor for the detection circuit $Q_{\text{det}} \sim 1000$, the detection-circuit linewidth is on the order of ~ 1 MHz and therefore larger than anharmonicity-induced broadening of the electron signal, as we show below. To reach the strong quantum regime, however, we require $Q_{\text{det}} \gg 7000$ (see Table I). However, with a tunable coupler [75,115], we could potentially tune the quality factor of the detection circuit to accommodate for both Q -factor regimes. Detailed analysis of such a coupler is beyond the scope of this paper. Therefore, in this section and in Sec. VI F, we use the lower $Q_{\text{det}} \sim 1000$ value.

Figure 17 shows the schematics of a typical tank detection circuit and Fig. 18 shows a simplified equivalent circuit. The simplification follows first from replacing the trapped electron with its BVD equivalent network L_e, C_e and a current source I_e corresponding to the induced currents due to electron motion. Further simplification is achieved by replacing the entire network connected to the two ends of the detection inductor L_{det} with its total equivalent capacitance C_{total} . This will define the tank circuit resonant frequency $\omega_0 = 1/\sqrt{L_{\text{det}} C_{\text{total}}}$, which we assume to be resonant with the electron trap frequency. Finally, the amplification network that couples to L_{det} via mutual inductance to the coupling inductor L_{cpl} is replaced by an equivalent resistor R_{det} . The coupling inductor L_{cpl} transduces the input impedance of the amplifier, the real part of which presents an effective resistance R_{ext} in parallel with the internal resistance R_{int} of the LC tank circuit. The total resistance of the detection circuit is therefore $R_{\text{det}} = R_{\text{ext}} R_{\text{int}} / (R_{\text{ext}} + R_{\text{int}})$. The width of the electron signal can be estimated to be $R_{\text{det}}/L_e \sim 2\pi \times 100$ kHz, expressed in terms of the trap parameters

$$\frac{R_{\text{det}}}{L_e} = \frac{Q_{\text{det}} q_e^2 \alpha^2}{\omega_0 C_{\text{total}} m_e d^2}, \quad (39)$$

where $d \sim 200$ μm is the endcap-to-endcap distance, $\omega_0 = 2\pi \times 1$ GHz is the trap secular motion frequency, and $C_{\text{total}} \sim 180$ fF for the trap in Fig. 14(b). The capacitance C_{total} is

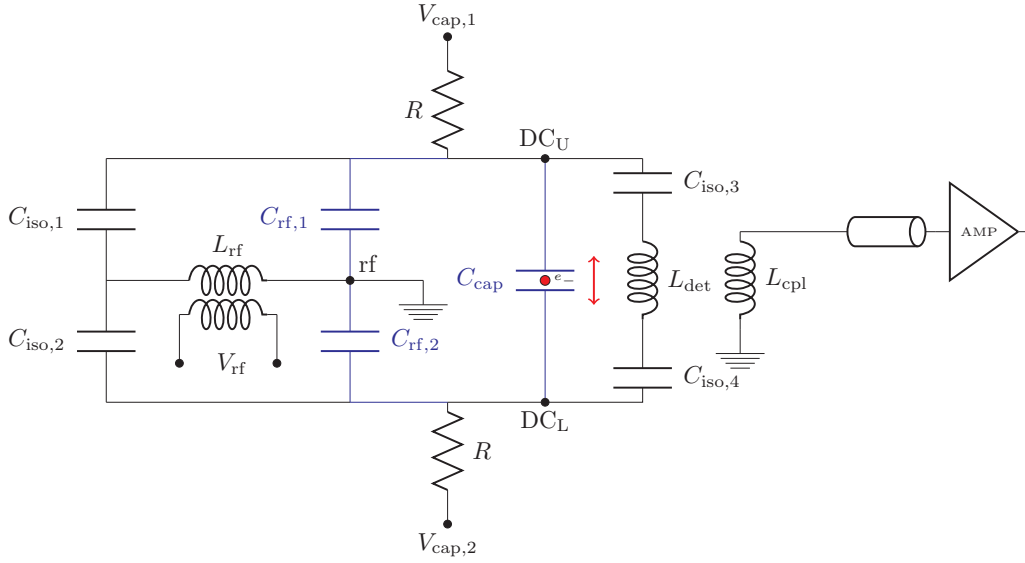


FIG. 17. Schematic of trap and detection resonators for the traps illustrated in Fig. 14. The electrodes DC_U , DC_L , and rf of Fig. 14 are indicated here in the schematic. The trap capacitances are shown in blue where $C_{rf,1}$ and $C_{rf,2}$ are the capacitances between the center ring and each endcap and C_{cap} is the endcap-to-endcap capacitance. For the trap in Fig. 14(a), these equal 21.3, 21.3, and 4.6 fF, respectively. For the trap in Fig. 14(b), these equal 146, 146, and 35 fF, respectively. The L_{rf} inductor forms a resonator with the total capacitance between its ends generating the quadrupole trapping field. The L_{det} inductor along with the capacitance shown forms the detection resonator that monitors the electron motion (double red arrow). The four isolation capacitors enable independent dc biasing of the upper and lower endcaps ($V_{cap,j}$, $j = 1, 2$) with bias resistors $R \geq 10 \text{ M}\Omega$ to avoid loading the detection circuit, assumed to have a quality factor of ~ 1000 [see Sec. VIE]. The leftmost isolation capacitors $C_{iso,1}$ and $C_{iso,2}$ are chosen to equal $C_{rf,1} = C_{rf,2}$. The rightmost isolation capacitors $C_{iso,3}$ and $C_{iso,4}$ are chosen to be much greater than the total capacitance between DC_L and DC_U , e.g., on the order of 1 pF. The mutual inductance of L_{det} and L_{cpl} allows for electron detection using an amplifier.

calculated by expressing it in terms of the other capacitances in Fig. 17 as

$$C_{total} = C_{cap} + \frac{C_{rf,1}C_{rf,2}}{C_{rf,1} + C_{rf,2}} + \frac{C_{iso,1}C_{iso,2}}{C_{iso,1} + C_{iso,2}}, \quad (40)$$

assuming that $C_{iso,k}$ ($k = 3, 4$) are much larger than C_{trap} .

While $C_{rf,k}$, $k = 1, 2$ and C_{cap} are dictated by the trap electrodes, $C_{iso,k}$, $k = 1, 2$ can be chosen independently. There is an inherent tradeoff in this choice, however. On the one hand,

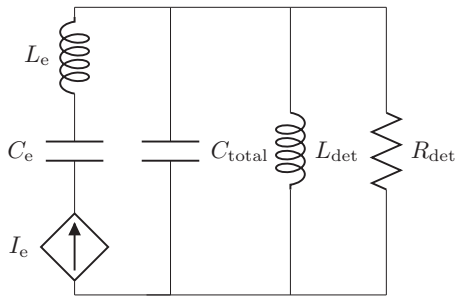


FIG. 18. Simplified electron-detection circuit, based on the circuit in Fig. 17. Here, C_{total} is the total capacitance between the two ends of the detection inductor L_{det} . The trapped electron is replaced by its electrical equivalent of a series LC resonator with inductance L_e and capacitance C_e . Currents generated by electron motion are represented by I_e . The coupling inductor L_{cpl} in Fig. 17 transduces the input impedance of the amplifier to an effective resistance, which, combined with LC internal dissipation, are represented by an equivalent shunt resistor R_{det} .

these should be much larger than $C_{rf,k}$ in order to maximize the trap drive voltage. On the other hand, these should be as small as possible so as to minimize C_{trap} and increase the coupling rate g . For simplicity, here we choose $C_{iso,1} = C_{iso,2} = C_{rf,1} = C_{rf,2}$ but other choices could be explored. For the trap in Fig. 17(a), $C_{total} \sim 26 \text{ fF}$, so $R_{det}/L_{ion} \sim 2\pi \times 0.7 \text{ MHz}$. See the caption of Fig. 17 for the capacitance values for both traps. The relatively large difference between the signal bandwidths calculated above and the typical signal bandwidth in a Penning trap experiment follows from the small dimensions and small capacitance of the designs considered here.

The width of the electron signal should be compared with the frequency spread resulting from the trap anharmonicity. By using first-order perturbation theory, we can estimate the effects of the r^4 , r^2z^2 , z^4 terms in the trap potential (see, for example, Ref. [80]) resulting in $\leq 0.5 \text{ MHz}$ dispersion in the signal for both traps in Fig. 14, assuming the electron thermal motion equilibrates to a 4 K bath. This should contribute very little to the broadening of a single-electron signal, thereby simplifying its detection without the need for a more elaborate electrode design. Notice also that the $\leq 0.5 \text{ MHz}$ dispersion falls within the bandwidth of the detection circuit described above, rendering the cooling induced by coupling to the detection circuit to be effective for electrons with temperatures $\leq 4 \text{ K}$ (energies $\leq 0.34 \text{ meV}$). Even in the presence of nonlinearities, a single electron could be detected by parametrically driving its motion and coherently detecting the resulting image currents in the detection circuit [16].

The bandwidths calculated above fall in between 0.1 and 1 MHz, and therefore correspond to a single-electron detection

time of 1 to 10 μs . By integrating the thermal power spectral density at R_{det} over a bandwidth of $B \equiv R_{\text{det}}/(2\pi L_e)$ centered at ω_0 , the total detected power will vary from $P_{\text{det}} \sim 4k_bTB$ when no electron is trapped to $P_{\text{det}} \sim 0$ when an electron is trapped [31]. This is a result of the fact that, on resonance, the electron equivalent circuit is effectively a short which shunts R_{det} , as seen in Fig. 18. To avoid a large noise background, an amplifier with an effective noise temperature that is $\leq T$ is required. As an example, for the $T = 4$ K experiments explored here, using an amplifier with a noise temperature of 2 K at $\omega_0/2\pi \sim 1$ GHz such as in Ref. [118] could suffice, giving an estimated signal-to-noise ratio of unity or larger in determining the variation in P_{det} before and after trapping.

F. Parametric cooling

The low-energy electron source described in Sec. VIC relies on the ability to cool the motion in all three spatial axes. As described there, adequate z -motion cooling can be achieved when the detection circuit is resonant with the z motion. By parametrically coupling the radial x and y motion to the z motion, cooling on all axes can be achieved [114]. Such a scheme has the benefit of not needing an extra radial electrode for damping or additional resonant circuitry on the existing ring electrode.

The coupling scheme in Ref. [114] was based on xy and xz terms in the pseudopotential, which were proportional to a voltage U . Time modulating $U(t) = U_0 \cos(\Delta\omega t)$ at the difference frequency $\Delta\omega = \omega_i - \omega_j$ causes energy exchange between the motion along the i and j axes. The traps considered in Fig. 14, however, are axially symmetric and therefore should have negligibly small cross terms of that type. We could also consider this approach by modifying the electrodes to be able to induce couplings of this form. Alternatively, a variation on this coupling scheme could be used that incorporates the symmetry of the simpler electrode structures. To see this, we approximate the trap pseudopotential around its minimum as

$$\phi_{\text{pseudo}} = \frac{1}{2}m_e(\omega_x^2x^2 + \omega_y^2y^2 + \omega_z^2z^2) + \beta x^2z^2 + \gamma y^2z^2, \quad (41)$$

where the x^2y^2 anharmonic term is also negligible for the axially symmetric traps considered and $\beta \approx \gamma$. In terms of the harmonic ladder operators, the x^2z^2 cross term, for example, contains the following summands:

$$\hbar\xi(a^2b^{\dagger 2} + b^2a^{\dagger 2}), \quad (42)$$

where a , a^\dagger are the z -motion operators and b , b^\dagger are the x -motion counterparts. Coherently driving the z motion at $\omega_d = 2\omega_x - \omega_z$ can be described mathematically by replacing $a \mapsto \alpha e^{-i\omega_d t} + a$. Rewriting Eq. (42) and neglecting fast rotating terms introduces terms of the form

$$2\hbar\xi\alpha(ab^{\dagger 2} + b^2a^\dagger). \quad (43)$$

As an example, consider the trap design in Fig. 14(a). There, in order to achieve x - z coupling, ω_d should be $\sim 2\pi \times 90$ MHz. By expressing β in terms of the pseudopotential parameters,

$$\beta = \zeta \frac{2q_e^2 V_{\text{rf}}^2}{m_e \Omega_{\text{rf}}^2 d^6}, \quad (44)$$

where $\zeta = 0.166$ is a geometric prefactor, we can express the x - z coupling frequency as

$$2\xi\alpha = \zeta \frac{\sqrt{2\hbar}q_e^3 V_{\text{rf}}^2 V_d}{m_e^{3.5} \Omega_{\text{rf}}^2 \omega_x \omega_z^{2.5} d^7}, \quad (45)$$

where V_d is the drive voltage applied to the trap endcaps. For the trap in Fig. 14(a), we get a rate of $2\pi \times 0.92$ MHz/V $\times V_d$. Therefore, a $V_d \sim 109$ mV drive, corresponding to ~ 3.36 μm of motion amplitude, would render an x - z coupling rate of $2\pi \times 100$ kHz. This would enable cooling of the x motion on the order of that rate. With a Q factor of 1000 for the detection circuit, a 109 mV drive at $\omega_d \sim 2\pi \times 90$ MHz would dissipate less than 10 nW of power, well within the cryogenic capabilities of the refrigerator.

G. Planar arrangements

Planar chip traps have some advantages over the three-dimensional traps analyzed above. They can be easier to fabricate, require no alignment, and are more suited for scalability. Such traps, however, have a much shallower trapping potential for the same applied voltages and frequencies, as compared with three-dimensional traps. This can be mitigated by adding a cover electrode a few millimeters away from the trap chip, and applying a negative voltage [82, 119, 120].

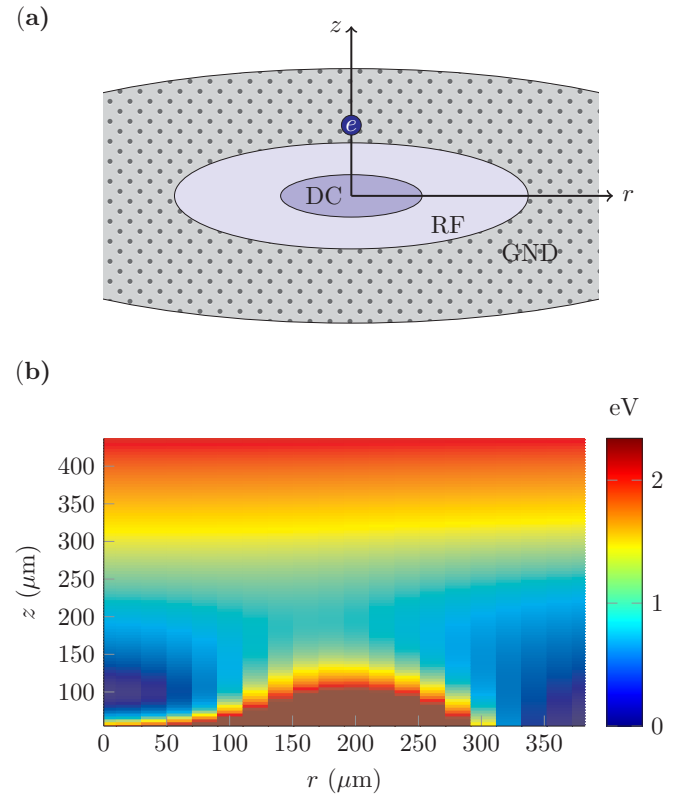


FIG. 19. Planar point Paul trap for electrons. (a) Inner DC disk radius is 100 μm . Outer RF ring radius is 250 μm . The electron is trapped at a height of ~ 100 μm above the surface. (b) Pseudopotential trap depth of the trap in panel (a), with 100 V trap drive at 7.1 GHz and a capping electrode, here represented by adding a uniform field of 58.5 V/cm along $-z$. The trap minimum is at $r = 0$, $z \sim 100$ μm . Resulting secular frequency along z is $\omega_z = 2\pi \times 1.46$ GHz.

Figure 19 shows an example of a planar electrode Paul trap [119,121], here chosen to be cylindrically symmetric for simplicity. With the addition of a cover electrode generating a uniform field of 58.5 V/cm, the trap depth is $D = 0.02q V_{\text{rf}} q_{\text{mathieu}}$. When applying a trap drive voltage of $V_{\text{rf}} = 100$ V to the RF annulus electrode (DC and GND electrodes are rf grounded) and assuming a Mathieu parameter of $q_{\text{mathieu}} \sim 0.5$, we expect a 1 eV trap depth, as in the three-dimensional designs shown earlier. The relevant trap capacitance that dictates the value of the coupling rate g is formed between the central dc electrode and ground. Due to the trap geometric aspect ratio, the coupling rate decreases to $g = 2\pi \times 180$ kHz. As a side effect of using a cover electrode, the electron equilibrium position should shift towards the trap chip by $7.7 \mu\text{m}$. This would result in $\sim 2 \mu\text{m}$ micromotion amplitude (corresponding to a pseudopotential energy of ~ 15 meV) that should be compatible with a stable trap operation. This, however, would compromise electron loading into the trap due to the additional rf heating resulting from excess micromotion (see Sec. VIC). One remedy could be to compensate for micromotion by applying dc voltages on the center DC electrode. In the example considered here, 1.5 V of dc bias would restore the ion position to the rf-null point, while still rendering a 1.6-eV-deep trap.

Although planar traps seem promising, separating the detection circuit from the drive circuit would be more difficult due to the lack of symmetry assumed in Sec. VID. Also, since planar traps tend to be more anharmonic compared with three-dimensional ones, additional compensation electrodes may be required in order to enable single-electron detection [82].

VII. CONCLUDING REMARKS

We first consider coupling the motion of a confined charged particle to a superconducting resonator. Limited by the currently achieved quality factors of such resonators ($Q \leq 10^6$), we conclude that, for the systems considered, it will be very difficult to reach the strong-coupling regime by using a single trapped charged particle, with perhaps the exception of ${}^9\text{Be}^+$ at dilution-refrigerator temperatures or trapped electrons.

We explored coupling a trapped ion to a nanomechanical resonator, either through electrostatics or piezoelectricity. Based on recent advances in the fabrication of membranes ($Q \geq 10^8$), we considered their electrostatic coupling to a trapped ion. By coating such a membrane with a thin metallic film and applying a voltage bias to it, the coupling could be on the order of 10 Hz for a 1 V bias, within reach of the strong-quantum regime at $T = 50$ mK.

We analyzed the possibility of direct piezoelectric coupling of ion motion to a mechanical resonator. An interesting candidate was a quartz acoustic resonator with a very high quality factor ($Q > 10^9$). However, due to the relatively small overlap between the ion electric field and the acoustic-mode shape, the coupling strength is found to be on the order of 1 Hz. Reshaping the ion field with the aid of a capacitor led to an increase in the coupling, to 10 Hz, approaching the strong quantum regime.

By laser cooling a single ${}^9\text{Be}^+$ ion that interacts with the quartz resonator, the acoustic mode with an effective mass of

≥ 1 mg (!) could be cooled close to its ground state of motion. If such a massive object is placed in a superposition state, it could be used to restrict various macroscopic decoherence theories. For example, quantum gravity has been suggested to result in a motional decoherence rate that is proportional to M^2 for an object of mass M [122]. If a few-milligram mechanical oscillator is placed in a superposition of position states differing by twice its zero-point motion, that superposition would decohere in ~ 10 ps. This effect should be testable since the expected coherence time of the quartz resonator is much longer, even at 4 K. To be well within the strong quantum regime, we could engineer a different resonator, perhaps with stronger piezoelectric coefficients, that maintains a high Q factor and where the acoustic-mode shape has a large overlap with the ion electric field. Such a task, however, is not straightforward because these different demands may not be compatible.

Lastly, we considered coupling an electron to a superconducting electrical resonator. We examined two specific trap designs with a 1 eV trap depth, a depth we view as crucial for initial trapping where laser cooling is not available. The relatively high voltages and currents required to create such a trap depth suggest the need for thick niobium conductors to form the trap, in order to maintain superconductivity. Additionally, a 1 eV trap requires a low-energy source of electrons, and damping to combat heating. We examined a three-dimensional trap arrangement, which can separate the high voltage, high current rf trapping circuitry from the low voltage, low currents flowing in the electron detection circuit by using trap symmetry. Obtaining a similar effect for a planar-chip trap geometry would be more complicated due to the lack of symmetry.

It is worth noting the appealing properties that a hybrid system based on a trapped electron might have. Such an architecture might be more scalable compared with trapped ion QIP since the interconnecting elements are chip based, requiring only rf control and no optical elements or laser beams. The absence of optical elements could allow for smaller traps, enabling stronger coupling between electrons and superconducting elements. Moreover, as the speed of entangling gates based on the Coulomb interaction of two charged particles scales with the trapping frequency, and as a trap for electrons would typically have secular frequencies that are two orders of magnitude larger than for ions, we expect shorter electron gate times as compared with trapped ions [69]. Recent advances in entangling trapped ions have reached gate speeds that are only an order of magnitude slower than the trap frequency [9]. If that were to scale for a trapped electron, it would correspond to a ~ 10 – 100 ns gate time, comparable to superconducting qubit gate times [72]. Electron spin-coherence times can exceed a second [73] and therefore be orders of magnitude larger than coherence times for superconducting qubits, where the best values to date are close to a millisecond [123]. Therefore, a hybrid QIP platform based on trapped electrons might have a much larger qubit coherence time to gate time ratio. The platform might offer an additional way to entangle electrons, mediated by the underlying circuitry. This would enrich the QIP toolbox available for electron spins. For this second method, gate speed is limited to the exchange rate between the electron and its accompanying superconducting resonator, which we estimate

to be on the order of $g \sim 2\pi \times 1$ MHz for 50 μm distance between electrons and superconducting circuitry and faster for smaller traps.

ACKNOWLEDGMENTS

The authors would like to thank K. Cicak for her help in estimating the coupling of an ion to a membrane and for her help with electron trap design and resulting fabrication constraints. We thank K. Bertness for discussions regarding GaN nanobeams. We thank M. Goryachev, S. Galliou, and M. E. Tobar for introducing us to the physics of BVA resonators as well as lending us devices to measure. We thank A. Sanders for introducing us to electron source and electron optics technology and for his help in assessing their relevance. We thank F. Lecocq, J. D. Teufel, and J. Aumentado for discussions regarding the superconducting and rf measurement aspects of this manuscript. We thank A. Sirois and D. Allcock for carefully reading this manuscript and their helpful comments. We appreciate support of the NIST Quantum Information program.

APPENDIX A: CALCULATING QUARTZ RESONATOR TO ION COUPLING

Coupling calculations require knowing the quartz resonator mode shape \vec{s} , the orientation of the crystallographic axes of the resonator, the corresponding 3×6 piezoelectric coefficient matrix of quartz e , and the ion electric field. We focus on the high- Q modes [Eq. (24)] that are quasilongitudinal, i.e., along the $\hat{n} = (0.226, 0.968, 0.111)$ unit vector, in the coordinate system described in Fig. 20. The BVA quartz resonators are made from doubly rotated SC (stress-compensated) cut quartz [62]. The coefficient matrix e for this cut is taken from Table 7 in the IEEE standard of piezoelectricity [124].

Denote the overlap integral in the numerator of Eq. (24) by g_c , i.e.,

$$g_i = \frac{\int_V d^3r \partial_i E_{\text{ion}} e s'}{2\omega_0 \sqrt{M m_{\text{ion}}}} \equiv \frac{g_c}{2\omega_0 \sqrt{M m_{\text{ion}}}}, \quad i = x, y, z. \quad (\text{A1})$$

The mode mass is calculated by the integral

$$\begin{aligned} M &= \int_V d^3r \rho_{\text{quartz}} |s|^2 \\ &= \rho_{\text{quartz}} \pi \sigma^2 \frac{t}{2} (1 - e^{-L^2/\sigma^2}), \end{aligned} \quad (\text{A2})$$

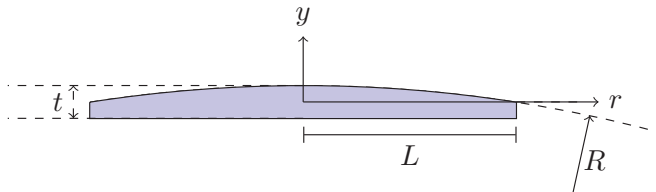


FIG. 20. BVA geometry. Cylindrically symmetric about the y axis with a maximal thickness t . The BVA lower surface is a flat disk of radius L . The BVA upper surface can be described by a curved surface $y = t(1 - \frac{r^2}{2Rt})$ with a radius of curvature R . We consider a resonator (not to scale) with $R = 300$ mm, $L = 6.5$ mm, $t = 1.08$ mm.

where σ is the Gaussian profile radial scale of the mode shape \vec{s} . From Ref. [66],

$$\sigma = \left(\frac{Rt^3}{3n^2\pi^2} \right)^{1/4}, \quad (\text{A3})$$

where $R = 300$ mm is the radius of curvature of the upper surface of the resonator, t is its thickness, and n is the mode number (see Fig. 20). An approximate formula for the resonance frequency is

$$\omega_0 = c_{\text{sound}} \frac{n\pi}{t}, \quad (\text{A4})$$

where $c_{\text{sound}} = 6750$ m/s is the speed of sound for the quasi-longitudinal modes.

An exact calculation of g_c can be found in Appendix A.2. Before doing so, we first estimate in Appendix A.1 an upper bound on g_c and correspondingly g , by avoiding the vector nature of the overlap integrand.

1. Upper bound on direct ion-quartz coupling

An upper bound can be obtained by using the Cauchy-Schwarz inequality applied to g_c :

$$\begin{aligned} g_c &= \int d^3r \partial_i E_{\text{ion}} e u' \\ &\leq \sqrt{\int d^3r (\partial_i E_{\text{ion}})^2} \sqrt{\int d^3r (e u')^2} \\ &\leq \sqrt{\int d^3r (\partial_i E_{\text{ion}})^2 e_{\text{max}}^2} \sqrt{\int d^3r (u')^2}, \end{aligned} \quad (\text{A5})$$

where $e_{\text{max}} \approx 0.234$ C/m² is the square root of the maximal eigenvalue of $e^\dagger e$. The electric field of an ion hovering at a height h along the \hat{y} axis is $E_{\text{ion}}(\vec{r}) \approx q\vec{R}/4\pi\epsilon R^3$ where $\vec{R} = \vec{r} - h\hat{y}$ and ϵ is the average dielectric constant of vacuum and quartz. We can therefore write

$$g_c \leq \gamma \frac{e_{\text{max}} q}{4\pi\epsilon\sqrt{h^3}} \sqrt{\int d^3r (u')^2}, \quad (\text{A6})$$

where γ is a numerical factor of order unity for all $i = x, y, z$ directions.

To estimate the last integral of the strain $(u')^2$, recall that the mode mass $M = \int d^3r \rho_{\text{quartz}} u^2$, where $\rho_{\text{quartz}} = 2.6 \times 10^3$ kg/m³ is the quartz density. Due to the mode shape [Eq. (24)] we may approximate $u' \sim ku$, where k is the wave number of the longitudinal oscillations within the BVA, i.e., $kt = n\pi$ for t the resonator thickness and $n = 1, 3, 5, \dots$. Therefore, $\int d^3r (u')^2 \sim k^2 \int d^3r u^2$ and we may estimate an upper bound,

$$\begin{aligned} g &\equiv \frac{g_c}{2\omega_0 \sqrt{M m_{\text{ion}}}} \\ &\leq \gamma \frac{e_{\text{max}} q}{4\pi\epsilon c_s \sqrt{m_{\text{ion}} \rho_{\text{quartz}} h^3}} \sim 2\pi \times 1 \text{ kHz}, \end{aligned} \quad (\text{A7})$$

where $c_s = 6757$ m/s is the speed of sound for the quasilongitudinal mode.

TABLE III. Direct coupling of a ${}^9\text{Be}^+$ ion to a BVA quartz resonator. The ion is assumed to be trapped $50\ \mu\text{m}$ above the quartz. The quartz thickness is assumed to be $1.08\ \text{mm}$. Coupling strength g_i for $i = x, y, z$ corresponds to an ion motion along the i axis. The longitudinal mode number is n .

n	Frequency	g_y	g_x	g_z
3	9.4 MHz	$2\pi \times 1.46\ \text{Hz}$	$2\pi \times 1.09\ \text{Hz}$	$2\pi \times 0.49\ \text{Hz}$
5	15.6 MHz	$2\pi \times 1.39\ \text{Hz}$	$2\pi \times 1.02\ \text{Hz}$	$2\pi \times 0.47\ \text{Hz}$
7	21.9 MHz	$2\pi \times 1.33\ \text{Hz}$	$2\pi \times 0.97\ \text{Hz}$	$2\pi \times 0.44\ \text{Hz}$
9	28.1 MHz	$2\pi \times 1.28\ \text{Hz}$	$2\pi \times 0.94\ \text{Hz}$	$2\pi \times 0.43\ \text{Hz}$

2. Direct ion-quartz-coupling calculation

Now that the upper bound has been established, we numerically calculate the integral in Eq. (A1) for the low-frequency modes of the quartz resonator (Table III). We see that all coupling strengths are below $1.5\ \text{Hz}$.

It is interesting to notice the weak dependence of the coupling strengths on the mode number n . Due to the frequency and mode mass scaling, the denominator of Eq. (A1) scales like \sqrt{n} . On the other hand, because the derivative of the ion field is equivalent to a dipole field, the integrand of g_c scales as $1/r^3$ whereas its Jacobian scales as $r\,dr$ so overall we should expect a $1/r \sim 1/\sigma \sim \sqrt{n}$ dependence, which nearly cancels the similar dependence in the denominator for the expression in g . Although, for very high frequency modes, g should deteriorate due to high spatial frequency averaging of the ion field.

3. Ion-quartz coupling via shunt capacitor

In the body of the paper, we estimate the coupling of the ion to the quartz resonator via a shunt capacitor by using a BVD equivalent electrical circuit. The main advantage of that approach, other than its simplicity, is that the effective capacitance of a BVA quartz resonator is a rather easily measured quantity [67].

Here, we use Eq. (A1) to directly calculate the coupling strength, in order to infer its dependence on mode parameters. To this end, we have to introduce parameters that describe the geometry involved. The ion is assumed to be trapped at the center of a parallel plate capacitor whose plates are a distance d_T from one another (see Fig. 21). The quartz resonator is

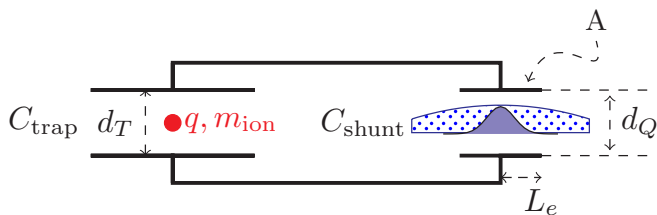


FIG. 21. Coupling an ion to a quartz resonator mediated by a shunt capacitor. An ion is elastically trapped (trap electrodes not shown) at the center of a parallel plate capacitor. The ion motion generates image currents that in turn generate an electric field between the parallel plate capacitor (each plate with area $A = \pi L_e^2$) encapsulating the quartz resonator.

assumed to be enclosed in another parallel plate capacitor, with a distance d_Q between the plates and a plate area of A .

If the ion is displaced by Δy from equilibrium towards one of the plates, it will generate an image charge $q^* = \Delta y q / d_T$. A portion of these image charges spread uniformly on the BVA shunt capacitor plates, creating a charge density $\sigma = q^* / A(1 + C_{\text{trap}} / C_{\text{shunt}})$ and exerting a field inside the BVA volume $E = \sigma / \epsilon$. We get

$$\frac{dE}{d\Delta y} = \frac{q}{\epsilon A d_T (1 + C_{\text{trap}} / C_{\text{shunt}})}, \quad (\text{A8})$$

where C_{trap} is the trap capacitance, and C_{shunt} is the BVA shunt capacitance and the field is perpendicular to the plates. As before, we focus on the quasilongitudinal mode shapes [Eq. (24)]. Performing the overlap integral in this case results in

$$g_c = \frac{4q\bar{e}\sigma^2}{\epsilon d_T L_e^2} (1 - e^{-L_e^2/2\sigma^2}) \frac{1}{1 + \frac{C_{\text{trap}}}{C_{\text{shunt}}}}, \quad (\text{A9})$$

where L_e is the electrode radius, \bar{e} is the mode-shape weighted average of $e_{22}, e_{2,4}, e_{26}$, i.e., $\bar{e} = n_y e_{22} + n_z e_{24} + n_x e_{26} = 7.43 \times 10^{-2}\ \text{C/m}^{-2}$ and $\hat{n} = (n_x, n_y, n_z) = (-0.23, -0.97, 0.1)$ is the quasilongitudinal mode direction vector. By maximizing g_c as a function of L_e and for $C_{\text{trap}} = 50\ \text{fF}$ trap capacitance, we estimate $L_e = 1.05\sigma$, so the coupling rate is

$$g = \frac{0.58q\bar{e}}{\epsilon d_T \omega_0 \sqrt{M m_{\text{ion}}}} = 2\pi \times 10\ \text{Hz}, \quad (\text{A10})$$

where we assumed coupling to a ${}^9\text{Be}^+$ ion, trapped between capacitor plates a distance $d_T = 200\ \mu\text{m}$ away from one another.

To see the geometric scaling of this, recall that $\sigma = (\frac{t^3 R}{3\pi^2 n^2})^{\frac{1}{4}}$ and $\omega_0 \approx c_s n\pi / t$ [66]. We get

$$g \approx 0.3 \frac{q\bar{e}}{\epsilon c_s \sqrt{m_{\text{ion}} \rho_{\text{quartz}}}} \frac{1}{d_T (tR/2)^{\frac{1}{4}} \sqrt{n}}. \quad (\text{A11})$$

From Eq. (A11), we expect the coupling to diminish for higher modes (increasing n). The dependence in the geometrical parameters t, R is also very weak ($1/4$ exponent) with values limited to thicknesses in the range of 0.5 to $1\ \text{mm}$ and radii of curvature in the $R \sim 300\ \text{mm}$ range.

APPENDIX B: ESTIMATING ELECTRON “ANOMALOUS” MOTIONAL HEATING RATE FROM AMBIENT NOISE

We estimate the “anomalous” heating rate of the electron motion by extrapolating from known ion heating rates [125–127]. If n denotes the average number of motional quanta in a trap with frequency f then

$$\dot{n} \propto \frac{q^2}{m} \frac{1}{d^4 f^{1+\alpha}}, \quad (\text{B1})$$

where q, m are the particle charge and mass, respectively, and α varies between 0.5 and 2 in various experiments. In this expression, d is the distance of the charge from the nearest electrode and we assume the electric-field noise is generated by independent fluctuating patch potentials of extent $< d$ [125].

TABLE IV. Selected measured heating rates \dot{n} for ion traps. Ion-to-surface distance is d , f is the trap frequency.

Trap material	T	ion	d	f	\dot{n}	Ref.
Au on sapphire	5 K	$^{88}\text{Sr}^+$	50 μm	1.32 MHz	4 quanta/s	[128]
Au on quartz	300 K	$^9\text{Be}^+$	40 μm	3.6 MHz	58 quanta/s	[129]
Nb on sapphire	6 K	$^{88}\text{Sr}^+$	100 μm	1 MHz	2 quanta/s	[91]

From Table IV and Eq. (B1) we can estimate the electron heating rate to be between 30 to 160 quanta/s for a trap-to-electron distance of $\sim 50 \mu\text{m}$ and an electron motional frequency of ~ 1 GHz, assuming $\alpha = 0.5$. For $\alpha = 2$, all of the extrapolated heating rates are below 0.02 quanta/s. These rates are at least three orders of magnitude smaller than the coupling rates we expect between the electron and the superconducting resonator. Specifically, with the traps considered in this paper, the coupling rates were estimated to be in the range of 0.18 to 1.06 MHz.

APPENDIX C: ELECTRON HEATING RATE DUE TO INCOMING ELECTRONS DURING THE LOADING PROCESS

We estimate an upper bound for the heating rate of trapped electrons due to collisions with incoming electrons during trap loading. We assume that a single electron is trapped in a three-dimensional harmonic potential with ~ 1 GHz secular frequency in all axes with a trap depth of $U_{\text{depth}} = 1$ eV. Incoming electrons, each having $E_p = 30$ eV of kinetic energy, collide with the trapped electron, causing heating.

We focus on a single trapped electron collision process since we are aiming at a steady-state number of just one to a few trapped electrons. Moreover, we assume that the trapped electron interacts with just one incoming electron at a time. This is consistent with the incoming electron current values we considered in Sec. VIC and the timescale for the collision process (see below).

We ignore the trap dynamics during any single collision since the former is relatively slow compared with the latter. To see this, first note that the timescale for a collision process is $b/v_{p,0}$ where b is the impact parameter and $v_{p,0}$ is the incoming electron initial velocity. The impact parameter is limited by the overall incoming electron beam radius r_0 , which we assume is $< 100 \mu\text{m}$. The incident electron speed is $v_{p,0} = \sqrt{2E_p/m_e} = 3.2 \times 10^6$ m/s where m_e is the electron mass. Therefore, the collision duration times are $\leq 3 \times 10^{-11}$ s, i.e., shorter than the trap drive period ($\sim 10^{-10}$ s) and much shorter than the trap harmonic period ($\sim 10^{-9}$ s). Based on our trap parameters, we can estimate that, during a collision, trap forces will change the positions of the two electrons by no more than $\sim 20\%$ as compared with a collision where no trap is involved. Since we are interested only in an order-of-magnitude estimate, we ignore these deviations from a trap-free calculation.

For our purposes, however, the trap still plays a role in determining the initial conditions of the collision process. Trapped electrons have an initial energy below U_{depth} . For simplicity we assume that the initial energy distribution is uniform in the range $0 \leq E_{s,0} \leq U_{\text{depth}}$ (see, for example,

Fig. 5 in Ref. [109]). The incoming electron, at the moment of entrance into the trapping region, either accelerates or decelerates prior to the collision, depending on the phase of the trap drive. For concreteness we use the geometry in Fig. 14(b), the trap parameters of Table II, and assume that the incoming electron velocity is initially along the trap symmetry axis z . The incoming electron's initial kinetic energy prior to collision will be spread by ± 15 eV around $E_p = 30$ eV, as we show later. Since the primary electron beam is initially aligned parallel to the rf electric field, the rf-trap-induced spread in E_p is maximal. If, for example, the electrons come at an angle of $\sim 54.7^\circ$ with respect to z , the energy spread in E_p reduces to ± 2.5 eV. At this angle, to first order, the rf-trap field lines are perpendicular to the incoming electrons' initial velocity. Our choice of geometry and electron direction therefore accentuates the spread in E_p due to the rf in order to fully appreciate its influence on the heating rate. Another effect of the trap is electron deflection in the transverse direction resulting in a rastering of the incoming beam. It can be shown by using elementary electrostatic consideration that the beam radius will expand by $\leq \exp\{2 \arcsin [q_e V_{\text{rf}} / (E_p + eV_{\text{rf}})]\} < 4$. Therefore, we must make sure that the initial beam diameter is small enough such that the beam does not strike the trap electrodes from rastering.

We assume that the process can be reasonably captured by classical mechanics. We therefore ignore the spins of the electrons, as well as scattering interference effects. The ratio between the quantum-mechanical differential cross section for electron-electron Coulomb scattering $(d\sigma/d\Omega)_{\text{quantum}}$ and its classical counterpart $(d\sigma/d\Omega)_{\text{classical}}$ can be bounded by $0.5 < |(d\sigma/d\Omega)_{\text{quantum}} / (d\sigma/d\Omega)_{\text{classical}}| < 1.03$, based on our parameters; see, e.g., Ref. [130]. The quantity of interest is the energy gain per collision, ΔE , which is the average of the energy gained per scattering direction over an appropriate range of solid angle. Therefore, our classical estimation of ΔE will also not deviate from a full quantum-mechanical estimation by more than the above bounds.

The geometry of a collision process is shown in Fig. 22(a). An incoming electron with velocity $\vec{v}_{p,0}$ and position \vec{r}_p collides with a relatively slow trapped electron (the target electron) with velocity $\vec{v}_{s,0}$ and position \vec{r}_s . Our subscripts follow the convention of electron scattering terminology where the incoming electrons are called "primary" whereas the (possibly) scattered electrons are called "scattered." The scattering problem can be described in the center-of-mass and reduced-mass coordinates: $R_{\text{c.m.}} \equiv (\vec{r}_p + \vec{r}_s)/2$, and $\vec{r} \equiv \vec{r}_p - \vec{r}_s$, respectively. Ignoring the trapping potential as mentioned above, we can assume that the center of mass will move at a constant velocity of $\vec{V}_{\text{c.m.}} = (\vec{v}_{p,0} + \vec{v}_{s,0})/2$. The relative motion is described in the primed coordinate system shown in Fig. 22(b). It is subsequently reduced to a Rutherford scattering problem of a particle of one electron charge and a reduced mass of $\mu = m_e/2$, moving with an initial velocity $\vec{v} = \vec{v}_{p,0} - \vec{v}_{s,0}$ and an impact parameter b , in the Coulomb potential of a fixed electron at the origin [see Fig. 22(b)]. The relative velocity vector will therefore be deflected with respect to its initial direction by

$$\theta_R = 2 \arctan \left(\frac{q_e^2 / 4\pi \epsilon_0 b}{\mu v^2} \right), \quad (\text{C1})$$

where $v \equiv |\vec{v}|$.

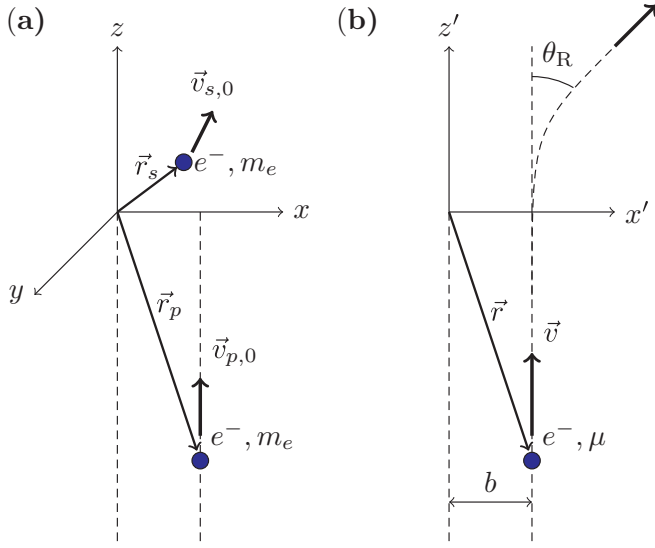


FIG. 22. Geometry of electron-electron scattering. (a) Laboratory frame. An incoming fast electron with velocity $\vec{v}_{p,0}$ collides with a slow (trapped) electron with velocity $\vec{v}_{s,0}$. (b) Reduced-mass frame of reference. Here, $\vec{r} \equiv \vec{r}_p - \vec{r}_s$, $\vec{v} \equiv \vec{v}_{p,0} - \vec{v}_{s,0}$, and $\mu = m_e/2$ is the reduced mass. The angle θ_R is the deflection angle of \vec{v} with respect to its initial direction, after the collision.

Returning to the laboratory frame, the target electron final velocity is

$$\vec{v}_s = \frac{\vec{v}_{p,0} + \vec{v}_{s,0}}{2} - \frac{\vec{v} \cos \theta_R + v \hat{u} \sin \theta_R}{2}, \quad (\text{C2})$$

where

$$\hat{u} = \frac{\vec{r} - (\vec{r} \cdot \hat{v})\hat{v}}{|\vec{r} - (\vec{r} \cdot \hat{v})\hat{v}|}, \quad \hat{v} = \frac{\vec{v}}{v}. \quad (\text{C3})$$

By using Eq. (C2) and the triangle inequality, we can find an upper bound for $|\vec{v}_s|$ as

$$\begin{aligned} |\vec{v}_s| &\leq |\vec{v}_{p,0} - \vec{v}_{s,0}| \left| \sin \frac{\theta_R}{2} \right| + |\vec{v}_{s,0}| \\ &\leq \left(1 + \sqrt{\frac{E_{\text{thresh}}}{E_p}} \right) |\vec{v}_{p,0}| \left| \sin \frac{\theta_R}{2} \right| + |\vec{v}_{s,0}|, \end{aligned} \quad (\text{C4})$$

where E_{thresh} is the maximal energy of an initially trapped electron (see Sec. VIC). This translates into a bound on the change in the kinetic energy of the target electron

$$\begin{aligned} |\Delta E| &= \left| \frac{1}{2} m_e |\vec{v}_s|^2 - \frac{1}{2} m_e |\vec{v}_{s,0}|^2 \right| \\ &\leq \gamma E_p \left| \sin \frac{\theta_R}{2} \right|, \end{aligned} \quad (\text{C5})$$

where

$$\gamma = \left(1 + \sqrt{\frac{E_{\text{thresh}}}{E_p}} \right) \left(1 + 3 \sqrt{\frac{E_{\text{thresh}}}{E_p}} \right). \quad (\text{C6})$$

If we use U_{depth} as a bound for E_{thresh} , we get $\gamma \approx 1.83$. However, in Sec. VIC we showed that only electrons with $E_{\text{thresh}} = 0.3$ meV are expected to be trapped, corresponding

to $\gamma \approx 1.01$. The average change in the absolute value of the target electron kinetic energy is therefore

$$\langle |\Delta E| \rangle \leq \gamma \frac{q_e^2}{4\pi\epsilon_0 r_0}, \quad (\text{C7})$$

where r_0 is the incoming electron beam radius. Here, we averaged over all possible impact parameters b , assuming that the incoming electrons are uniformly distributed in an electron beam having a radius of r_0 :

$$\begin{aligned} \left\langle \gamma E_p \left| \sin \frac{\theta_R}{2} \right| \right\rangle &= \frac{\gamma E_p}{2r_0^2} \int_0^{2r_0} db b \frac{1}{\sqrt{1 + \left(\frac{2\pi\epsilon_0 b m_e v^2}{q_e^2} \right)^2}} \\ &\approx \frac{\gamma E_p}{2r_0^2} \int_0^{2r_0} db b \frac{1}{\sqrt{1 + \left(\frac{4\pi\epsilon_0 b E_p}{q_e^2} \right)^2}} \\ &\approx \gamma \frac{q_e^2}{4\pi\epsilon_0 r_0}, \end{aligned} \quad (\text{C8})$$

where the approximation $v \sim v_p$ was used.

A subtle point in the calculation of the average in Eq. (C8) is the assumption of a uniformly distributed (spatial) incident electron beam. While this assumption is reasonable in the laboratory frame, it is not immediately clear that it is adequate for the center-of-mass frame. For trapped electrons with an initial energy $\leq E_{\text{thresh}} = 0.3$ meV; that is, significantly smaller than $E_p = 30$ eV, the assumption of uniformity is a good approximation since the laboratory frame and center-of-mass frame are nearly identical. The value of E_{thresh} might be larger if measures are taken to decrease trap anharmonicity. The ultimate bound for E_{thresh} is therefore U_{depth} . In that case, we can see numerically that going to the center-of-mass frame

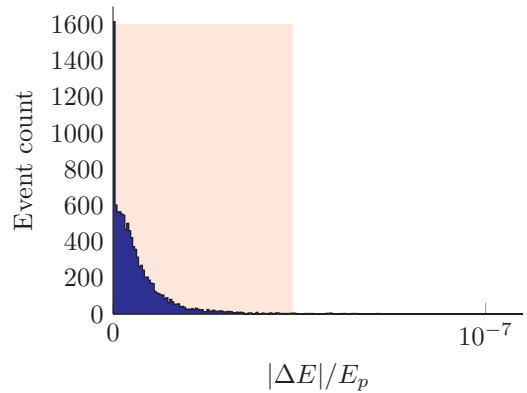


FIG. 23. Histogram of the absolute value of the change in total energy of a trapped electron, $|\Delta E|$, due to collisions with an $E_p = 30$ eV incoming electrons. Shaded pink region shows the analytic bound in Eq. (C7). We numerically integrate the equations of motion for an electron, trapped initially at $x = y = z = 0$, with initial energy E_s , interacting with the incoming electron. We assume a pseudopotential harmonic trap with 1 GHz frequencies in all axes in a trapping volume of $l^3 = (95 \mu\text{m})^3$. Here we do not account for micromotion dynamics. The energy E_s is assumed to be uniformly distributed between $0 \leq E_s \leq U_{\text{depth}} = 1.01$ eV and the incoming electron position is assumed to be at $z = -1$ mm with x, y uniformly distributed in the beam cross section, $(x^2 + y^2)^{1/2} \leq r_0 = 100 \mu\text{m}$.

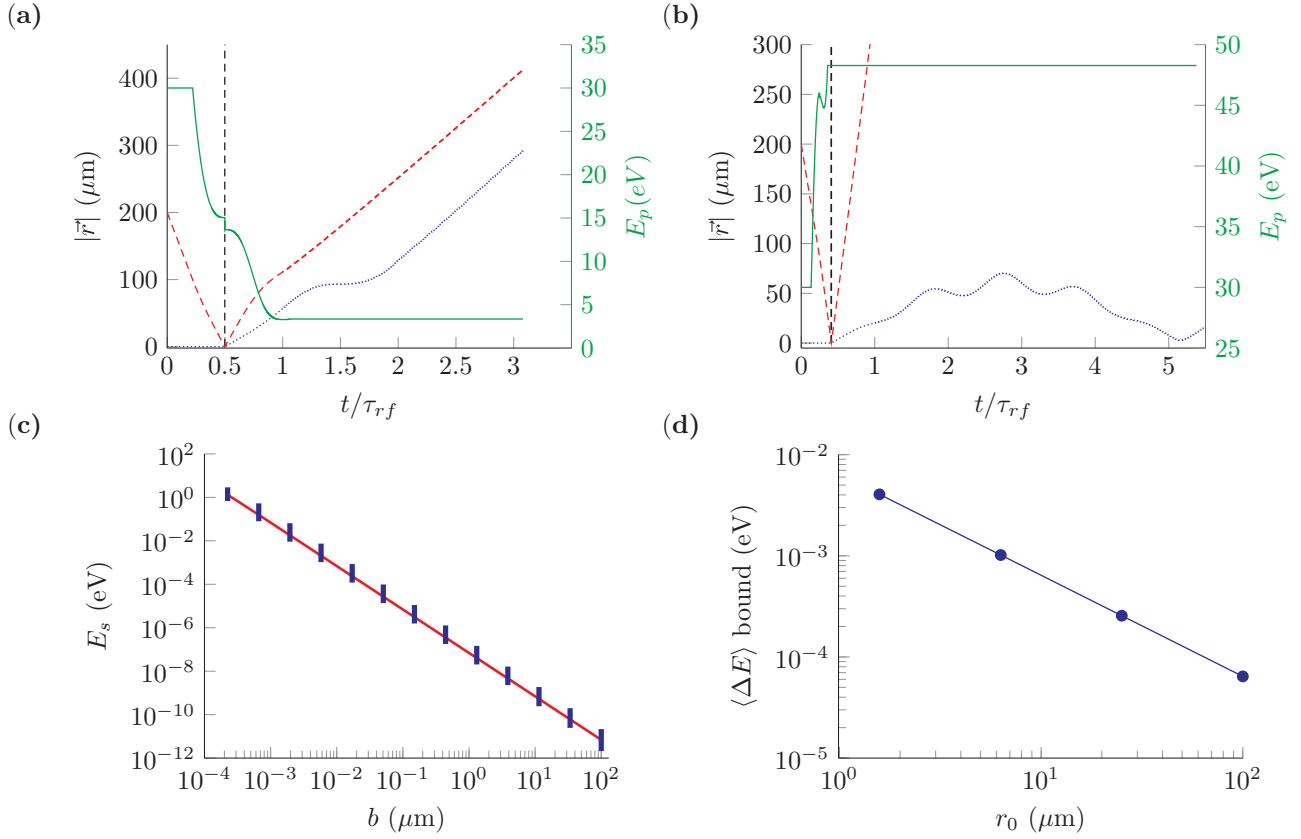


FIG. 24. The effect of micromotion on electron-electron scattering for a harmonic trap with dimensions and frequencies similar to those described in Fig. 14(b). (a) Example of a simulated trajectory of a trapped electron (dotted blue curve) colliding with an incoming electron (dashed red curve) at an impact parameter $b = 10 \text{ \AA}$, as a function of time in units of the trap rf period τ_{rf} . Trap center is assumed at the origin $x = y = z = 0$ and \vec{r} is the particle position. The instantaneous kinetic energy of the incoming electron E_p (solid green curve) decreases prior to the collision due to the varying rf potential. When the incoming electron is at a distance of the order of $\sim b$ from the trap center (dashed black line), the incoming electron loses 1.39 eV giving the trapped electron enough energy to escape the trap. (b) Same as panel (a), but for an initial rf phase shifted by π radians as compared to panel (a). In this case, the trapped electron gains 0.27 eV due to the collision, resulting in confined oscillations. (c) Blue vertical lines show the spread in the final target electron energy E_s vs impact parameter b , resulting from different initial trap rf phases. Analytic theory of Eq. (C10) is shown by the solid red line. (d) Bound on the average energy gain per collision vs incoming electron beam radius r_0 . Target electron initial kinetic energy is assumed to be uniformly distributed from 0 eV to 1 eV. Analytic theory of Eq. (C8) (solid blue line) is compared with a numerical integration of Eq. (C11) that includes the spread in impact parameters and incoming electron kinetic energies due to micromotion (blue circles). The spread in these values is calculated by numerical integration of the equations of motion for the two electrons, for various initial conditions, and under the influence of the trap rf field as well as their Coulomb repulsion. Initial conditions are assumed uniform as in Fig. 23.

redistributes the impact parameters to include a larger range of distances and consequentially a lower average impact energy. The calculation in Eq. (C8) can therefore be regarded as an upper bound on the actual average value of $|\sin(\theta_R/2)|$. As an example, we compare this bound to a histogram of $|\Delta E|$ derived from a numerical integration of the collision equation of motion for a random set of initial conditions, as seen in Fig. 23. The target electron energy before collision $E_{s,0}$ is assumed to be uniformly distributed $0 \leq E_{s,0} \leq U_{\text{depth}}$. The incoming electron beam is assumed to be uniformly distributed. From the histogram, the average absolute value of the energy imparted to the target electron per collision is $\sim 0.74 \times 10^{-7} E_p$. Assuming $0 \leq E_{s,0} \leq U_{\text{thresh}}$, this average decreases to $\sim 10^{-9} E_p$. Both values are consistent with the analytic expression in Eq. (C7) which yields a bound of $4.8 \times 10^{-7} E_p$. The simulation is set up to account for the effect of the trapping pseudopotential during the collision process, thereby serving as an independent

validation of the omission of trap dynamics in our analytic derivation.

Since the bound in Eq. (C7) does not depend on the target electron initial velocity, it can be translated to a corresponding average heating rate bound by multiplying it by the incoming rate of electrons. A current density of J incoming electrons results in $J\pi r_0^2/q_e$ collisions per second, which in turn results in a heating rate bound of

$$\left(\frac{dE}{dt}\right)_e \leq \frac{q_e J r_0}{4\epsilon_0}, \quad (\text{C9})$$

where we approximated $\gamma \approx 1$.

The above discussion did not include the effect of micromotion on the collisions. The effect of the trap drive is to spread the kinetic energy of the incoming electron as well as the impact parameter of the collision. The bound in Eq. (C9) changes only by a factor of order unity due to micromotion. To

see this, we first consider the simple case of a target electron initially at rest in the absence of rf fields. By using Eq. (C2) we can write the target electron exact final kinetic energy due to a single collision:

$$E_s = E_p \frac{x^2}{1+x^2}, \quad x \equiv \frac{q_e^2/4\pi\epsilon_0 b}{E_p}. \quad (\text{C10})$$

For $x \ll 1$ (equivalently $b \gg 1 \text{ \AA}$), faster (slower) incoming electrons result in a smaller (larger) increase of the target electron energy, $E_s \propto 1/E_p$.

In the presence of a rf trap, the incoming electron can either accelerate or decelerate before the collision, depending on the initial phase of the trap drive when it entered the trapping region. An accelerated (decelerated) electron will therefore transfer less (more) energy to the target electron as compared with the no-trap collision. This is exactly the case for the two examples shown in Figs. 24(a) and 24(b). These simulate collision processes for initial rf phases that differ by π radians. For concreteness, we assumed an rf trap with dimensions and frequencies as in Fig. 14(b) and Table II. We simplified the calculation by assuming the trap is harmonic in the entire cylindrical volume bounded by the electrodes. The incoming electron initial velocity is assumed to be parallel to the trap z axis. Figure 24(a) shows a collision process where the incoming electron is maximally decelerated to a kinetic energy of $E_p = 15 \text{ eV}$ at the beginning of the collision. This results in the ejection of the target electron from the trap. Figure 24(b) shows the other extreme case where the incoming electron experiences maximal acceleration resulting in $E_p = 46 \text{ eV}$ so the target electron remains trapped. Although this may seem paradoxical, it follows immediately from Eq. (C10) for impact parameters which satisfy $b \gg 1 \text{ \AA}$.

To see how well this explanation encapsulates the effect of micromotion for the general case, we compare the theory in Eq. (C10) to the values of E_s extracted from numerical simulations as a function the impact parameter b . We vary the values of b from 1 \AA , below which collisions are essentially head on [equivalently $x \sim 1$ in Eq. (C10)], to $100 \mu\text{m}$, i.e., the electron beam radius. For a given value of b , the different values of the trap initial rf phase result in the spread in E_s values shown in Fig. 24(c) (blue markers). The center of these distributions, however, follows the theory in Eq. (C10), which assumes no trap drive [solid red line in Fig. 24(c)]. Overall, the effect of micromotion is a $\sim 60\%$ spread in the value of E_s , centered at the value given by Eq. (C10).

Finally, we extend our treatment to include nonzero initial velocity for the target electron. To this end, we repeat the calculation in Eq. (C8) with the addition of averaging over the rf initial phase ϕ_{rf} :

$$\begin{aligned} & \left\langle \gamma E_p \left| \sin \frac{\theta_R}{2} \right| \right\rangle \\ &= \frac{\gamma}{2\pi r_0^2} \int_0^{r_0} db b \int_0^{2\pi} d\phi_{\text{rf}} \frac{E_{p,\text{col}}}{\sqrt{1 + \left(\frac{2\pi\epsilon_0 b_{\text{col}} m_e v^2}{q_e^2} \right)^2}}, \quad (\text{C11}) \end{aligned}$$

where $E_{p,\text{col}}$ and b_{col} are the impact energy and impact parameter at the time of collision and are functions of ϕ_{rf} . Numerical evaluations of Eq. (C11) are in good agreement with the analytic theory which assumed the absence of a trap [Eq. (C8)], as can be seen in Fig. 24(d). Here, the value of γ in Eq. (C6) changes to $\gamma \sim 2.23$ to account for the maximally decelerated incoming electrons, with energies as low as 15 eV .

-
- [1] W. Paul, *Rev. Mod. Phys.* **62**, 531 (1990).
 [2] H. Dehmelt, *Rev. Mod. Phys.* **62**, 525 (1990).
 [3] R. Blatt and D. J. Wineland, *Nature (London)* **453**, 1008 (2008).
 [4] D. Hanneke, J. P. Home, J. D. Jost, J. M. Amini, D. Leibfried, and D. J. Wineland, *Nat. Phys.* **6**, 13 (2010).
 [5] P. Schindler, D. Nigg, T. Monz, J. T. Barreiro, E. Martinez, S. X. Wang, S. Quint, M. F. Brandl, V. Nebendahl, C. F. Roos, M. Chwalla, M. Hennrich, and R. Blatt, *New J. Phys.* **15**, 123012 (2013).
 [6] C. Monroe and J. Kim, *Science* **339**, 1164 (2013).
 [7] C. Roos, in *Fundamental Physics in Particle Traps* (Springer, Berlin, Heidelberg, 2014), pp. 253–291.
 [8] T. P. Harty, D. T. C. Allcock, C. J. Ballance, L. Guidoni, H. A. Janacek, N. M. Linke, D. N. Stacey, and D. M. Lucas, *Phys. Rev. Lett.* **113**, 220501 (2014).
 [9] C. J. Ballance, T. P. Harty, N. M. Linke, M. A. Sepiol, and D. M. Lucas, *Phys. Rev. Lett.* **117**, 060504 (2016).
 [10] J. P. Gaebler, T. R. Tan, Y. Lin, Y. Wan, R. Bowler, A. C. Keith, S. Glancy, K. Coakley, E. Knill, D. Leibfried, and D. J. Wineland, *Phys. Rev. Lett.* **117**, 060505 (2016).
 [11] J. J. Bollinger, D. J. Heinzen, W. M. Itano, S. L. Gilbert, and D. J. Wineland, *IEEE Trans. Instrum. Meas.* **40**, 126 (1991).
 [12] P. T. H. Fisk, M. J. Sellars, M. A. Lawn, C. Coles, A. G. Mann, and D. G. Blair, *IEEE Trans. Instrum. Meas.* **44**, 113 (1995).
 [13] C. Langer, R. Ozeri, J. D. Jost, J. Chiaverini, B. DeMarco, A. Ben-Kish, R. B. Blakestad, J. Britton, D. B. Hume, W. M. Itano, D. Leibfried, R. Reichle, T. Rosenband, T. Schaetz, P. O. Schmidt, and D. J. Wineland, *Phys. Rev. Lett.* **95**, 060502 (2005).
 [14] K. Geerlings, S. Shankar, E. Edwards, L. Frunzio, R. J. Schoelkopf, and M. H. Devoret, *Appl. Phys. Lett.* **100**, 192601 (2012).
 [15] D. J. Heinzen and D. J. Wineland, *Phys. Rev. A* **42**, 2977 (1990).
 [16] D. J. Wineland, P. Ekstrom, and H. Dehmelt, *Phys. Rev. Lett.* **31**, 1279 (1973).
 [17] D. Kielpinski, D. Kafri, M. J. Woolley, G. J. Milburn, and J. M. Taylor, *Phys. Rev. Lett.* **108**, 130504 (2012).
 [18] N. Daniilidis, D. J. Gorman, L. Tian, and H. Häffner, *New J. Phys.* **15**, 073017 (2013).
 [19] D. Kafri, P. Adhikari, and J. M. Taylor, *Phys. Rev. A* **93**, 013412 (2016).
 [20] D. De Motte, A. R. Grounds, M. Reháč, A. Rodriguez Blanco, B. Lekitsch, G. S. Giri, P. Neilinger, G. Oelsner, E. Il'ichev,

- M. Grajcar, and W. K. Hensinger, *Quantum Inf. Process.* **15**, 5385 (2016).
- [21] D. J. Wineland, C. Monroe, W. M. Itano, D. Leibfried, B. E. King, and D. M. Meekhof, *J. Res. Natl. Inst. Stand. Technol. (U. S.)* **103**, 259 (1998).
- [22] L. Tian and P. Zoller, *Phys. Rev. Lett.* **93**, 266403 (2004).
- [23] W. K. Hensinger, D. W. Utami, H. S. Goan, K. Schwab, C. Monroe, and G. J. Milburn, *Phys. Rev. A* **72**, 041405 (2005).
- [24] D. Hunger, S. Camerer, M. Korppi, A. Jöckel, T. W. Hansch, and P. Treutlein, *C. R. Phys.* **12**, 871 (2011).
- [25] N. Daniilidis and H. Häffner, *Annu. Rev. Condens. Matter Phys.* **4**, 83 (2013).
- [26] N. Daniilidis, T. Lee, R. Clark, S. Narayanan, and H. Häffner, *J. Phys. B: At., Mol. Opt. Phys.* **42**, 154012 (2009).
- [27] K. R. Brown, C. Ospelkaus, Y. Colombe, A. C. Wilson, D. Leibfried, and D. J. Wineland, *Nature (London)* **471**, 196 (2011).
- [28] M. Harlander, R. Lechner, M. Brownnutt, R. Blatt, and W. Hänsel, *Nature (London)* **471**, 200 (2011).
- [29] G. Ciaramicoli, I. Marzoli, and P. Tombesi, *Phys. Rev. Lett.* **91**, 017901 (2003).
- [30] P. M. Platzman and M. I. Dykman, *Science* **284**, 1967 (1999).
- [31] D. J. Wineland and H. G. Dehmelt, *J. Appl. Phys.* **46**, 919 (1975).
- [32] S. Butterworth, *Proc. Phys. Soc. London* **26**, 264 (1913).
- [33] S. Butterworth, *Proc. Phys. Soc. London* **27**, 410 (1914).
- [34] K. S. Van Dyke, *Proc. Inst. Radio Eng.* **16**, 742 (1928).
- [35] M. D. Sirkis and N. Holonyak, *Am. J. Phys.* **34**, 943 (1966).
- [36] D. Leibfried, R. Blatt, C. Monroe, and D. J. Wineland, *Rev. Mod. Phys.* **75**, 281 (2003).
- [37] M. Aspelmeyer, T. J. Kippenberg, and F. Marquardt, *Rev. Mod. Phys.* **86**, 1391 (2014).
- [38] J. Wenner, R. Barends, R. C. Bialczak, Y. Chen, J. Kelly, E. Lucero, M. Mariantoni, A. Megrant, P. J. J. O'Malley, D. Sank, A. Vainsencher, H. Wang, T. C. White, Y. Yin, J. Zhao, A. N. Cleland, and J. M. Martinis, *Appl. Phys. Lett.* **99**, 113513 (2011).
- [39] D. M. Pozar, *Microwave Engineering*, 4th ed. (Wiley Global Education, Hoboken, 2011).
- [40] R. P. Erickson, M. R. Vissers, M. Sandberg, S. R. Jefferts, and D. P. Pappas, *Phys. Rev. Lett.* **113**, 187002 (2014).
- [41] J. M. Taylor (private communication).
- [42] B. M. Zwickl, W. E. Shanks, A. M. Jayich, C. Yang, A. C. B. Jayich, J. D. Thompson, and J. G. E. Harris, *Appl. Phys. Lett.* **92**, 103125 (2008).
- [43] P. L. Yu, K. Cicak, N. S. Kampel, Y. Tsaturyan, T. P. Purdy, R. W. Simmonds, and C. A. Regal, *Appl. Phys. Lett.* **104**, 023510 (2014).
- [44] J. D. Teufel, *Physics* **9**, 147202 (2016).
- [45] C. Reinhardt, T. Müller, A. Bourassa, and J. C. Sankey, *Phys. Rev. X* **6**, 021001 (2016).
- [46] R. A. Norte, J. P. Moura, and S. Gröblacher, *Phys. Rev. Lett.* **116**, 147202 (2016).
- [47] Y. Tsaturyan, A. Barg, E. S. Polzik, and A. Schliesser, *arXiv:1608.00937*.
- [48] R. W. Andrews, R. W. Peterson, T. P. Purdy, K. Cicak, R. W. Simmonds, C. A. Regal, and K. W. Lehnert, *Nat. Phys.* **10**, 321 (2014).
- [49] W. G. Cady, *Piezoelectricity: An Introduction to the Theory and Applications of Electromechanical Phenomena in Crystals*, International Series in Pure and Applied Physics (McGraw-Hill, New York, 1946).
- [50] J. Chiaverini, R. B. Blakestad, J. Britton, J. D. Jost, C. Langer, D. Leibfried, R. Ozeri, and D. J. Wineland, *Quantum Inf. Comput.* **5**, 419 (2005).
- [51] S. Seidelin, J. Chiaverini, R. Reichle, J. J. Bollinger, D. Leibfried, J. Britton, J. H. Wesenberg, R. B. Blakestad, R. J. Epstein, D. B. Hume, W. M. Itano, J. D. Jost, C. Langer, R. Ozeri, N. Shiga, and D. J. Wineland, *Phys. Rev. Lett.* **96**, 253003 (2006).
- [52] R. Maiwald, D. Leibfried, J. Britton, J. C. Bergquist, G. Leuchs, and D. J. Wineland, *Nat. Phys.* **5**, 551 (2009).
- [53] C. L. Arrington, K. S. McKay, E. D. Baca, J. J. Coleman, Y. Colombe, P. Finnegan, D. A. Hite, A. E. Hollowell, R. Jördens, J. D. Jost, D. Leibfried, A. M. Rowen, U. Warring, M. Weides, A. C. Wilson, D. J. Wineland, and D. P. Pappas, *Rev. Sci. Instrum.* **84**, 085001 (2013).
- [54] J. D. Jackson, *Classical Electrodynamics*, 3rd ed. (Wiley, New York, 1999).
- [55] A. N. Cleland, *Foundations of Nanomechanics: From Solid-State Theory to Device Applications*, Advanced Texts in Physics (Springer, Berlin, 2003).
- [56] S. M. Tanner, J. M. Gray, C. T. Rogers, K. A. Bertness, and N. A. Sanford, *Appl. Phys. Lett.* **91**, 203117 (2007).
- [57] J. G. Gualtieri, J. A. Kosinski, and A. Ballato, *IEEE Trans. Ultrason. Ferroelectr. Freq. Control* **41**, 53 (1994).
- [58] S. S. Verbridge, J. M. Parpia, R. B. Reichenbach, L. M. Bellan, and H. G. Craighead, *J. Appl. Phys.* **99**, 124304 (2006).
- [59] M. Poot and H. S. J. van der Zant, *Phys. Rep.* **511**, 273 (2012).
- [60] S. Galliou, J. Imbaud, M. Goryachev, R. Bourquin, and P. Abbé, *Appl. Phys. Lett.* **98**, 091911 (2011).
- [61] M. Goryachev, D. L. Creedon, E. N. Ivanov, S. Galliou, R. Bourquin, and M. E. Tobar, *Appl. Phys. Lett.* **100**, 243504 (2012).
- [62] S. Galliou, M. Goryachev, R. Bourquin, P. Abbé, J. P. Aubry, and M. E. Tobar, *Sci. Rep.* **3**, 2132 (2013).
- [63] M. Goryachev, D. L. Creedon, S. Galliou, and M. E. Tobar, *Phys. Rev. Lett.* **111**, 085502 (2013).
- [64] M. Goryachev, E. N. Ivanov, F. van Kann, S. Galliou, and M. E. Tobar, *Appl. Phys. Lett.* **105**, 153505 (2014).
- [65] R. J. Besson, J. J. Boy, and M. M. Mourey, in *Proceedings of the 1995 IEEE International Frequency Control Symposium (49th Annual Symposium)* (San Francisco, 1995), pp. 590–599.
- [66] D. S. Stevens and H. F. Tiersten, *J. Acoust. Soc. Am.* **79**, 1811 (1986).
- [67] M. Goryachev, Ph.D. thesis, FEMTO-ST, 2011 (unpublished).
- [68] S. Galliou (private communication).
- [69] C. Ospelkaus, C. E. Langer, J. M. Amini, K. R. Brown, D. Leibfried, and D. J. Wineland, *Phys. Rev. Lett.* **101**, 090502 (2008).
- [70] C. Ospelkaus, U. Warring, Y. Colombe, K. R. Brown, J. M. Amini, D. Leibfried, and D. J. Wineland, *Nature (London)* **476**, 181 (2011).
- [71] P. Peng, C. Matthiesen, and H. Häffner, *Phys. Rev. A* **95**, 012312 (2017).
- [72] J. Kelly, R. Barends, A. G. Fowler, A. Megrant, E. Jeffrey, T. C. White, D. Sank, J. Y. Mutus, B. Campbell, Y. Chen, Z. Chen, B. Chiaro, A. Dunsworth, I. C. Hoi, C. Neill, P. J. J. O'Malley, C. Quintana, P. Roushan, A. Vainsencher, J. Wenner,

- A. N. Cleland, and J. M. Martinis, *Nature (London)* **519**, 66 (2015).
- [73] S. Kotler, N. Akerman, Y. Glickman, A. Keselman, and R. Ozeri, *Nature (London)* **473**, 61 (2011).
- [74] A. Sørensen and K. Mølmer, *Phys. Rev. A* **62**, 022311 (2000).
- [75] M. S. Allman, J. D. Whittaker, M. Castellanos-Beltran, K. Cicak, F. da Silva, M. P. DeFeo, F. Lecocq, A. Sirois, J. D. Teufel, J. Aumentado, and R. W. Simmonds, *Phys. Rev. Lett.* **112**, 123601 (2014).
- [76] J. D. Whittaker, F. C. S. da Silva, M. S. Allman, F. Lecocq, K. Cicak, A. J. Sirois, J. D. Teufel, J. Aumentado, and R. W. Simmonds, *Phys. Rev. B* **90**, 024513 (2014).
- [77] E. Jeffrey, D. Sank, J. Y. Mutus, T. C. White, J. Kelly, R. Barends, Y. Chen, Z. Chen, B. Chiaro, A. Dunsworth, A. Megrant, P. J. J. O'Malley, C. Neill, P. Roushan, A. Vainsencher, J. Wenner, A. N. Cleland, and J. M. Martinis, *Phys. Rev. Lett.* **112**, 190504 (2014).
- [78] F. Galve, P. Fernández, and G. Werth, *Eur. Phys. J. D* **40**, 201 (2006).
- [79] F. Galve and G. Werth, *Hyperfine Interact.* **174**, 41 (2007).
- [80] P. Bushev, S. Stahl, R. Natali, G. Marx, E. Stachowska, G. Werth, M. Hellwig, and F. Schmidt-Kaler, *Eur. Phys. J. D* **50**, 97 (2008).
- [81] L. S. Brown and G. Gabrielse, *Rev. Mod. Phys.* **58**, 233 (1986).
- [82] J. Goldman and G. Gabrielse, *Phys. Rev. A* **81**, 052335 (2010).
- [83] J. D. Goldman, Ph.D. thesis, Harvard University, 2011 (unpublished).
- [84] I. Marzoli, P. Tombesi, G. Ciaramicoli, G. Werth, P. Bushev, S. Stahl, F. Schmidt-Kaler, M. Hellwig, C. Henkel, G. Marx, I. Jex, E. Stachowska, G. Szawiola, and A. Walaszyk, *J. Phys. B: At., Mol. Opt. Phys.* **42**, 154010 (2009).
- [85] P. Bushev, D. Bothner, J. Nagel, M. Kemmler, K. B. Kononov, A. Loerincz, K. Ilin, M. Siegel, D. Koelle, R. Kleiner, and F. Schmidt-Kaler, *Eur. Phys. J. D* **63**, 9 (2011).
- [86] G. Yang, A. Fragner, G. Koolstra, L. Ocola, D. A. Czaplewski, R. J. Schoelkopf, and D. I. Schuster, *Phys. Rev. X* **6**, 011031 (2016).
- [87] A. J. Dahm, J. M. Goodkind, I. Karakurt, and S. Pilla, *J. Low Temp. Phys.* **126**, 709 (2002).
- [88] M. I. Dykman, P. M. Platzman, and P. Seddighrad, *Phys. Rev. B* **67**, 155402 (2003).
- [89] S. A. Lyon, *Phys. Rev. A* **74**, 052338 (2006).
- [90] D. I. Schuster, A. Fragner, M. I. Dykman, S. A. Lyon, and R. J. Schoelkopf, *Phys. Rev. Lett.* **105**, 040503 (2010).
- [91] S. X. Wang, Y. Ge, J. Labaziewicz, E. Dauler, K. Berggren, and I. L. Chuang, *Appl. Phys. Lett.* **97**, 244102 (2010).
- [92] J. Hoffrogge, R. Fröhlich, M. A. Kasevich, and P. Hommelhoff, *Phys. Rev. Lett.* **106**, 193001 (2011).
- [93] J. Walz, S. B. Ross, C. Zimmermann, L. Ricci, M. Prevedelli, and T. W. Hansch, *Phys. Rev. Lett.* **75**, 3257 (1995).
- [94] J. M. Amini, J. Britton, D. Leibfried, and D. J. Wineland, [arXiv:0812.3907](https://arxiv.org/abs/0812.3907).
- [95] J. C. Bergquist, D. J. Wineland, W. M. Itano, H. Hemmati, H. U. Daniel, and G. Leuchs, *Phys. Rev. Lett.* **55**, 1567 (1985).
- [96] M. A. Rowe, A. Ben-Kish, B. Demarco, D. Leibfried, V. Meyer, J. Beall, J. Britton, J. Hughes, W. M. Itano, B. Jelenkovic, C. Langer, T. Rosenband, and D. J. Wineland, *Quantum Inf. Comput.* **2**, 257 (2002).
- [97] J. W. Britton, J. P. Nibarger, K. W. Yoon, J. A. Beall, D. Becker, H.-M. Cho, G. C. Hilton, J. Hubmayr, M. D. Niemack, and K. D. Irwin, *Proc. SPIE* **7741**, 77410T (2010).
- [98] T. Van Duzer and C. W. Turner, *Principles of Superconductive Devices and Circuits*, 2nd ed. (Prentice Hall, Upper Saddle River, 1998).
- [99] C. C. Chin, D. E. Oates, G. Dresselhaus, and M. S. Dresselhaus, *Phys. Rev. B* **45**, 4788 (1992).
- [100] U. Weigel, Ph.D. thesis, Ruperto-Carola University of Heidelberg, 2003 (unpublished).
- [101] D. A. Orlov, U. Weigel, D. Schwalm, A. S. Terekhov, and A. Wolf, *Nucl. Instrum. Methods Phys. Res., Sect. A* **532**, 418 (2004).
- [102] S. Karkare, L. Cultrera, Y.-W. Hwang, R. Merluzzi, and I. Bazarov, *Rev. Sci. Instrum.* **86**, 033301 (2015).
- [103] G. F. Saville, J. M. Goodkind, and P. M. Platzman, *Phys. Rev. Lett.* **70**, 1517 (1993).
- [104] F. L. Walls and T. S. Stein, *Phys. Rev. Lett.* **31**, 975 (1973).
- [105] J. R. S. Van Dyck, P. B. Schwinberg, and H. G. Dehmelt, *Phys. Rev. Lett.* **38**, 310 (1977).
- [106] J. M. Sage, A. J. Kerman, and J. Chiaverini, *Phys. Rev. A* **86**, 013417 (2012).
- [107] F. Pobell, *Matter and Methods at Low Temperatures*, 2nd ed. (Springer, Berlin, 1996).
- [108] NIST Database, <http://www.nist.gov/pml/data/ionization/> Electron-impact ionization cross sections (2015).
- [109] J. Grissom, R. Compton, and W. Garrett, *Phys. Rev. A* **6**, 977 (1972).
- [110] T. W. Shyn and W. E. Sharp, *Phys. Rev. A* **19**, 557 (1979).
- [111] H. G. Dehmelt, *Adv. At. Mol. Phys.* **3**, 53 (1968).
- [112] H. G. Dehmelt, *Adv. At. Mol. Phys.* **5**, 109 (1969).
- [113] K. Shigemura, M. Kitajima, M. Kurokawa, K. Toyoshima, T. Odagiri, A. Suga, H. Kato, M. Hoshino, H. Tanaka, and K. Ito, *Phys. Rev. A* **89**, 022709 (2014).
- [114] D. J. Gorman, P. Schindler, S. Selvarajan, N. Daniilidis, and H. Häffner, *Phys. Rev. A* **89**, 062332 (2014).
- [115] Y. Yin, Y. Chen, D. Sank, P. J. J. O'Malley, T. C. White, R. Barends, J. Kelly, E. Lucero, M. Mariantoni, A. Megrant, C. Neill, A. Vainsencher, J. Wenner, A. N. Korotkov, A. N. Cleland, and J. M. Martinis, *Phys. Rev. Lett.* **110**, 107001 (2013).
- [116] E. C. Beaty, *Phys. Rev. A* **33**, 3645 (1986).
- [117] E. C. Beaty, *J. Appl. Phys.* **61**, 2118 (1987).
- [118] S. Weinreb, J. C. Bardin, and H. Mani, *IEEE Trans. Microwave Theory Tech.* **55**, 2306 (2007).
- [119] T. H. Kim, P. F. Herskind, T. Kim, J. Kim, and I. L. Chuang, *Phys. Rev. A* **82**, 043412 (2010).
- [120] R. Schmied, J. H. Wesenberg, and D. Leibfried, *New J. Phys.* **13**, 115011 (2011).
- [121] J. H. Wesenberg, *Phys. Rev. A* **78**, 063410 (2008).
- [122] O. Romero-Isart, *Phys. Rev. A* **84**, 052121 (2011).
- [123] M. Reagor, W. Pfaff, C. Axline, R. W. Heeres, N. Ofek, K. Sliwa, E. Holland, C. Wang, J. Blumoff, K. Chou, M. J. Hatridge, L. Frunzio, M. H. Devoret, L. Jiang, and R. J. Schoelkopf, *Phys. Rev. B* **94**, 014506 (2016).
- [124] A. H. Meitzler, D. Berlincourt, F. S. Welsh, and H. F. Tiersten, *IEEE Standard on Piezoelectricity: ANSI* (1987).
- [125] Q. A. Turchette, D. Kielpinski, B. E. King, D. Leibfried, D. M. Meekhof, C. J. Myatt, M. A. Rowe, C. A. Sackett, C. S. Wood,

- W. M. Itano, C. Monroe, and D. J. Wineland, *Phys. Rev. A* **61**, 063418 (2000).
- [126] D. A. Hite, Y. Colombe, A. C. Wilson, D. T. C. Allcock, D. Leibfried, D. J. Wineland, and D. P. Pappas, *MRS Bull.* **38**, 826 (2013).
- [127] M. Brownnutt, M. Kumph, P. Rabl, and R. Blatt, *Rev. Mod. Phys.* **87**, 1419 (2015).
- [128] J. Chiaverini and J. M. Sage, *Phys. Rev. A* **89**, 012318 (2014).
- [129] D. A. Hite, Y. Colombe, A. C. Wilson, K. R. Brown, U. Warring, R. Jördens, J. D. Jost, K. S. McKay, D. P. Pappas, D. Leibfried, and D. J. Wineland, *Phys. Rev. Lett.* **109**, 103001 (2012).
- [130] N. F. Mott and H. S. W. Massey, *The Theory of Atomic Collisions*, International series of monographs on physics, 3rd. ed. (Clarendon Press, Oxford, 1965); N. F. Mott, *Proc. R. Soc. London, Ser. A* **126**, 259 (1930).